

Chaotic system detection of weak seismic signals

Y. Li,¹ B. J. Yang,² J. Badal,³ X. P. Zhao,² H. B. Lin^{1,2} and R. L. Li²

¹Department of Information Engineering, Jilin University, Changchun 130026, China

²Department of Geophysics, Jilin University, Changchun 130026, China. E-mail: yangbaojun@jlu.edu.cn

³Physics of the Earth, Sciences B, University of Zaragoza, Pedro Cerbuna 12, Zaragoza 50009, Spain

Accepted 2009 April 27. Received 2009 April 27; in original form 2006 October 8

SUMMARY

When the signal-to-noise (S/N) ratio is less than -3 dB or even 0 dB, seismic events are generally difficult to identify from a common shot record. To overcome this type of problem we present a method to detect weak seismic signals based on the oscillations described by a chaotic dynamic system in phase space. The basic idea is that a non-linear chaotic oscillator is strongly immune to noise. Such a dynamic system is less influenced by noise, but it is more sensitive to periodic signals, changing from a chaotic state to a large-scale periodic phase state when excited by a weak signal. With the purpose of checking the possible contamination of the signal by noise, we have performed a numerical experiment with an oscillator controlled by the Duffing–Holmes equation, taking a distorted Ricker wavelet sequence as input signal. In doing so, we prove that the oscillator system is able to reach a large-scale periodic phase state in a strong noise environment. In the case of a common shot record with low S/N ratio, the onsets reflected from a same interface are similar to one other and can be put on a single trace with a common reference time and the periodicity of the so-generated signal follows as a consequence of moveout at a particular scanning velocity. This operation, which is called ‘horizontal dynamic correction’ and leads to a nearly periodic signal, is implemented on synthetic wavelet sequences taking various sampling arrival times and scanning velocities. Thereafter, two tests, both in a noisy ambient of -3.7 dB, are done using a chaotic oscillator: the first demonstrates the capability of the method to really detect a weak seismic signal; the second takes care of the fundamental weakness of the dynamic correction coming from the use of a particular scanning velocity, which is investigated from the effect caused by near-surface lateral velocity variation on the periodicity of the reconstructed seismic signal. Finally, we have developed an application of the method to real data acquired in seismic prospecting and then converted into pseudo-periodic signals, which has allowed us to discriminate fuzzy waveforms as multiples, thus illustrating in practice the performance of our working scheme.

Key words: Time series analysis; Spatial analysis; Computational seismology.

1 INTRODUCTION

Chaos theory was developed early and has been used in many fields: medicine (May 1974, 1976; May & Anderson 1979; Anderson & May 1982), solid-state physics (Teitsworth *et al.* 1983; Teitsworth & Westervelt 1984; Weiss *et al.* 1985; Moloney & Newell 1990), electronic counter measures (Simmendinger & Hess 1996), security in communications (Pecora & Carroll 1990, 1991; Bernhardt 1994; Short 1997) and also in seismic prospecting. Much of the recent works in this field focus on enhancement techniques and approaches to increase the signal-to-noise (S/N) ratio (Harris & White 1997; Selvi 1997; Linus *et al.* 1998; Quin & Smythe 1998; Ekren & Ursin 1999; Hung & Forsyth 2000; Jiao & Moon 2000; Kelamis & Verschuur 2000; Van der Baan & Paul 2000; Van der Heuvel *et al.* 2000; Freybourger & Chevrot 2001; Spitzer *et al.* 2001; Steeghs &

Drijkoningen 2001; Benyamin 2002; Soma *et al.* 2002; Brandsberg-Dahl *et al.* 2003; Tyapkin & Robinson 2003; Wang 2003; Boashash & Mesbah 2004; Jin *et al.* 2005). But few of these works concern the direct detection of weak signals or strongly contaminated signals by natural noise. This is the essential objective of the present work based on the behaviour of a non-linear chaotic oscillator in the phase space.

The topic of chaotic systems has been intensively studied in modern non-linear science due to their implications for weak signal detection. An experiment with chaotic oscillators aimed at signal detection in noise environments was performed by Birx (1992). Later, Haykin & Li (1995) utilized an artificial neural network to detect target weak signals contaminated by chaotic noise. Leung & Huang (1996) estimated the parameters of an autoregressive model affected by chaotic noise using the minimum phase space volume

approach. Wang *et al.* (1999) used chaotic oscillators for weak signal detection via the measurement of a sinusoidal signal perturbed by white noise, with an *S/N* ratio of -34 dB. More recently, Li & Yang (2003) have studied chaotic detection of harmonic and square waves affected by strong background noise being the *S/N* ratio about -60 dB.

In this study, the disturbance and sensitivity characteristics that control the periodic solutions of a chaotic oscillator system are used for weak signal detection. Based on the well-known immunity of a non-linear dynamic oscillator to noise, we check if it reaches a (stable) large-scale periodic phase state when excited by a nearly periodic signal. Even a weak signal of this type contaminated by unavoidable natural noise may influence the state of the system and induce significant phase changes because of its particular sensitivity. Consequently, if the signal of interest is assumed to be pseudo-periodic, one can investigate whether the signal really exists or

not by checking the state of the system in the phase space (Li & Yang 2003). The chaotic state of an oscillator system is completely different from its large-scale periodic phase state and therefore the shift from one to another is taken as the criterion for signal detection. It is a pre-condition of the signal detection method based on a chaotic system sensitive to weak signals. The key for detecting an input signal rests upon the identification of those phase changes. Therefore, the larger the difference between two configurations of the system in the phase space, the smaller the probability of error in the identification.

2 DETECTING WEAK PERIODIC SIGNALS

Previous theoretical analysis and simulation have demonstrated that the Duffing equation, equal to other motion equations that imply a

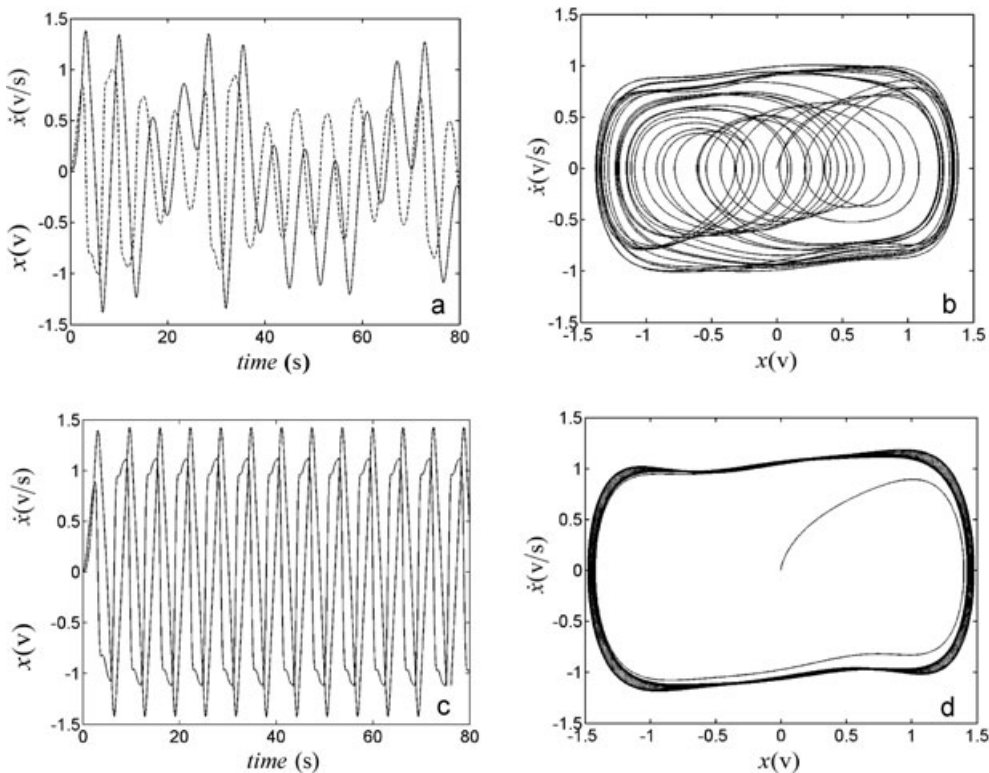


Figure 1. Upper part: Outputs corresponding to the oscillator system (eq. 3) in a chaotic state ($\gamma = 0.69$, $\omega = 1 \text{ rad s}^{-1}$): (a) variations of the displacement x (solid line) and \dot{x} (dashed line) with time; (b) orbits in a chaotic state. Lower part: The oscillator system in a large-scale periodic phase state ($\gamma = 0.72561713$, $\omega = 1 \text{ rad s}^{-1}$): (c) variations of the displacement x (solid line) and \dot{x} (dashed line) with time; (d) orbits in a large-scale periodic phase state.

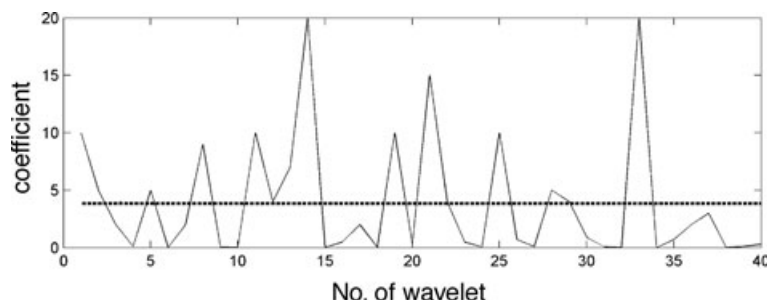


Figure 2. Values of the coefficients that distort a Ricker-type wavelet in amplitude; they are all joined by a polygonal linkage line. In total we have handled 40 coefficients varying in a broad range: two of them reach the maximum value of 20 and six have the minimum value of 0.01. The average value of the 40 coefficients is 3.88 (horizontal dot line).

deterministic method (Lorenz equation, Fandpul equation, etc.), results in chaotic behaviour of the physical system under its control when forced by periodic signals (Li & Yang 2003). The chaotic state is a particular solution of the non-linear equation that controls the physical system. However, different systems have different sensitivities to periodic signals when they evolve from a chaotic orbit state to a large-scale phase state. Let be a non-linear system described by the Duffing equation

$$\ddot{x} + k\dot{x} + \alpha x + \beta x^3 = 0, \quad (1)$$

where k is the viscous damping factor, $\alpha x + \beta x^3$ plays the role of non-linear elastic restitution depending on the displacement x and k , α , β are real numbers (the dot means derivation with respect to time). Under an external periodic force the Duffing equation becomes

$$\ddot{x} + k\dot{x} + \alpha x + \beta x^3 = \gamma \cos(\omega t), \quad (2)$$

γ and ω are the strength and the angular frequency of the external force, respectively. Distinct values of the coefficient γ determine chaotic or periodic orbits in the phase space, bifurcation points, etc. (Guckenheimer & Holmes 1983).

To acquire a chaotic detection system sensitive to any periodic signal, the Duffing equation must be reformulated. As the behaviour of a dynamic system lies in the (non-linear) restitution force once the input signal is fixed, we rewrite the non-linear part $\alpha x + \beta x^3$ under the assumption that the chaotic detection model is controlled by the equation

$$\ddot{x} + k\dot{x} - x^3 + x^5 = \gamma s(\omega t), \quad (3)$$

where $-x^3 + x^5$ is now the non-linear restitution term and $\gamma s(\omega t)$ is the input signal. Eq. (3) is a type of Duffing equation more appropriate to tackling sensitivity and stability aspects in the course

of our analysis (Li & Yang 2003). Here it is used for simulation of a chaotic oscillator system with viscous damping $k = 0.5$ and solved by the four-order Runge–Kutta algorithm, thus obtaining pairs $x(n+1)$, $y(n+1)$ at each time step, being $y(n) = \dot{x}(n)$. Once the value of the damping factor k is fixed in eq. (3), the system passes from chaotic state to describe periodic orbits as the coefficient γ changes (Fig. 1). After undergoing a transitory state, the system remains stabilized on a motion state and then it is easy to see whether the system is in chaotic state or in large-scale periodic state. Thus, it is possible to determine whether the input signal is noise or rather if it contains a weak periodic sinusoidal component.

Later, we shall assume that the signal of interest is $\gamma s(\omega t) + z_s$, which is introduced in eq. (3) as external periodic perturbation force: $\gamma s(\omega t)$ is the periodic amplitude component of the signal that can be adjusted by γ to reach a critical phase state, whereas z_s is random noise. Eq. (3) becomes

$$\ddot{x} + k\dot{x} - x^3 + x^5 = \gamma s(\omega t) + z_s, \quad (4)$$

and the change from chaotic state to periodic orbits allows us to determine if the input signal contains a sinusoidal component.

3 CHAOTIC DETECTION OF A RICKER WAVELET SEQUENCE

With the purpose of considering the possible contamination of the signal by noise, we have conducted a numerical experiment from a distorted Ricker wavelet sequence constructed by 40 Ricker wavelets:

$$R_n(t) = [1 - 2\pi^2 f_m^2(t - nT')^2] e^{-\pi^2 f_m^2(t - nT')^2} \\ f_m = 30 \text{ Hz}, \quad T' = 77 \text{ ms}, \quad n = 0, 1, \dots, 39. \quad (5)$$

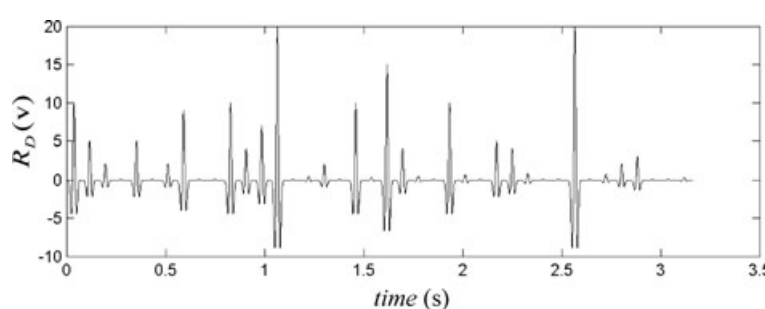


Figure 3. Distorted Ricker wavelet sequence taken for simulation and constructed with 40 wavelets modelled by distortion coefficients (Fig. 2). Any of these wavelets has a dominant frequency of 30 Hz and extends over a time window of 77 ms.

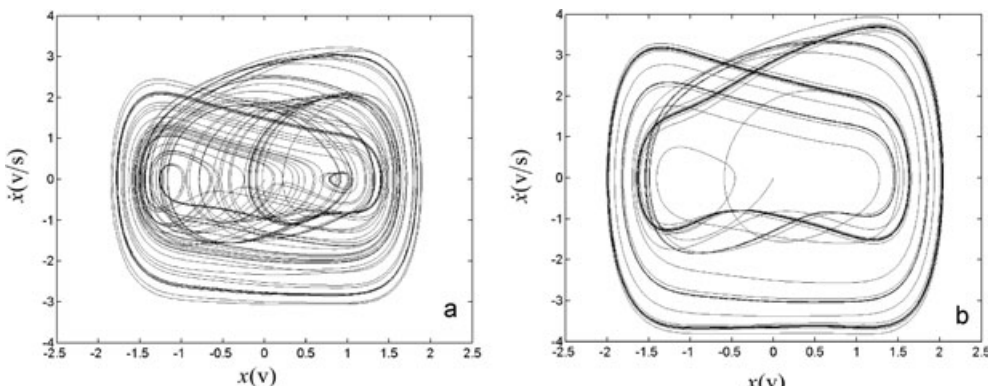


Figure 4. Orbits in the phase space described by the non-linear dynamic system controlled by eq. (9) (a) chaotic state and (b) periodic phase state.

All the wavelets are of the same type, but their respective amplitudes are distorted by 40 coefficients given by the vector $D = (10, 5, 2, 0.1, 5, 0.01, 2, 9, 0.06, 0.01, 10, 4, 7, 20, 0.03, 0.5, 2, 0.02, 10, 0.3, 15, 4, 0.5, 0.06, 10, 0.7, 0.1, 5, 4, 0.9, 0.08, 0.01, 20, 0.01, 0.7, 2, 3, 0.01, 0.1, 0.3)^T$. As Fig. 2 shows, these coefficients D_n have a broad range with $D_{\max} = 20$ (for D_{14} and D_{33}) and $D_{\min} = 0.01$ (for $D_6, D_{10}, D_{32}, D_{34}$ and D_{38}); thus, $D_{\max}:D_{\min} = 2000:1$. Each element D_n of the vector D acts on the n th wavelet R_n resulting in the distorted wavelet

$$R_n D_n, \quad n = 0, 1, \dots, 39. \quad (6)$$

The input signal is constructed as the sum of wavelets

$$R'_w = \sum_{n=0}^{39} R_n(t) \quad (7)$$

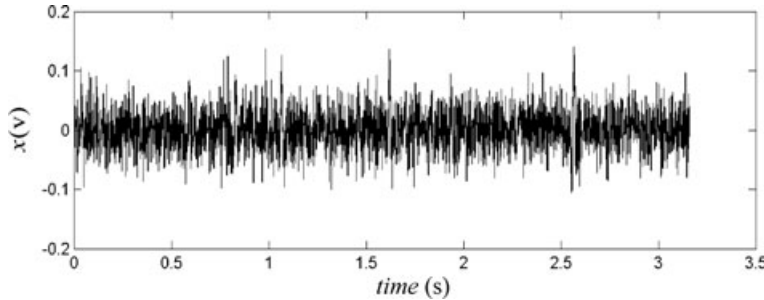


Figure 5. Signal consisting of the distorted Ricker wavelet train shown in Fig. 3 mixed with white noise, which is taken as input for simulation in the laboratory. The signal can hardly be distinguished from the noise.

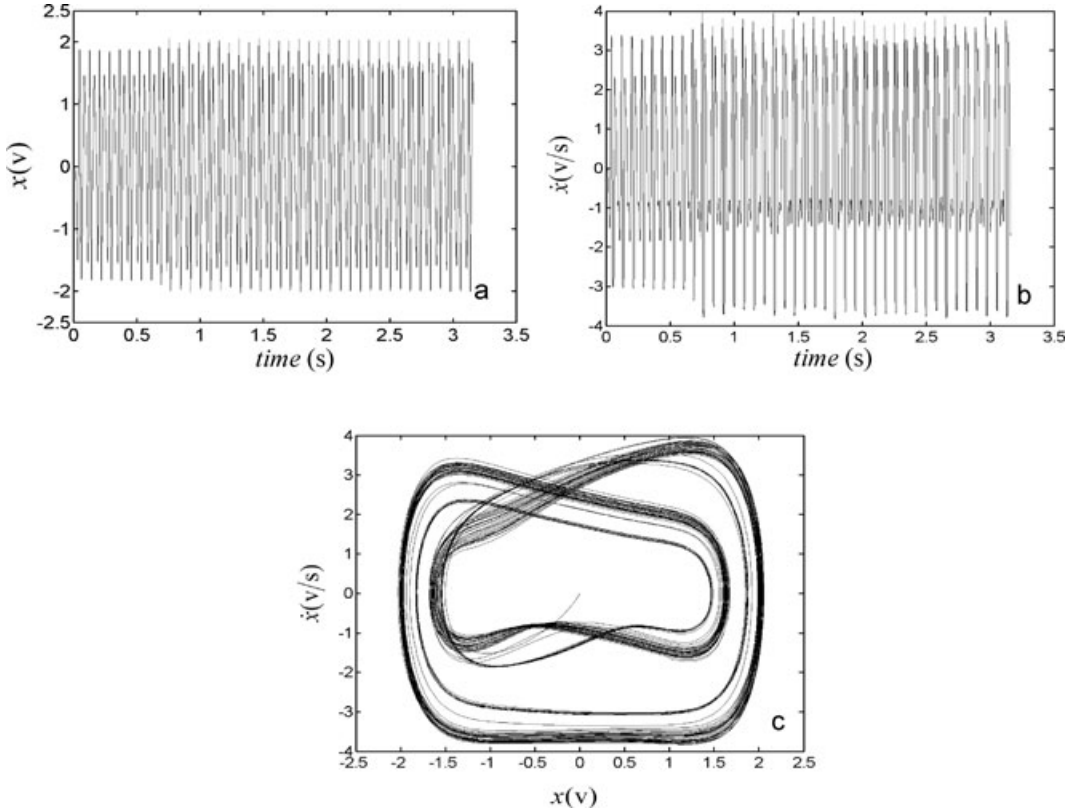


Figure 6. Solutions of the control eq. (9) obtained after adjusting the value of ξ : (a) displacement x ; (b) first-order derivative \dot{x} of the solution; and (c) orbits described by the non-linear dynamic system in the periodic phase state.

inserting two zeros between adjacent wavelets. Nevertheless, it is supposed that the oscillator system is affected by noise, and therefore, the distorted Ricker wavelet sequence is given by

$$R_D = R'_W D, \quad (8)$$

is used for simulation (Fig. 3).

According to eq. (4), the chaotic oscillator system used for detection is controlled by the equation

$$\ddot{x} + 0.5\dot{x} - x^3 + (1 + \xi R_D + z s)x^5 = \gamma R'_W, \quad (9)$$

where ξ is a coefficient permitting the adjustment of the amplitude of the distorted Ricker wavelet R_D . Setting $\xi = 0$ and assuming zero noise in eq. (9), the system goes from the chaotic phase state (Fig. 4a) to the critical phase state (Fig. 4b), with the critical value $A_L = 4.46021636$. If the mixed signal is now $\xi R_D +$ random noise (Fig. 5) and we solve eq. (9), which controls the behaviour

of the system, the oscillator is capable of reaching a large-scale periodic phase state (Fig. 6). In this case the coefficient ξ is $A_S = 5.5 \times 10^{-3}$ and the sampling time $\Delta t = 1$ ms, so that the average power of the distorted Ricker signal ξR_D is

$$\bar{P}_R = \frac{1}{40} \sum_{i=0}^{39} \left\{ \frac{1}{79\Delta t} \sum_{\substack{j=1 \\ t=j\Delta t}}^{79} \{[D_i A_s R_i(t)]^2 \Delta t\} \right\} = 1.63 \times 10^{-4} \text{W}. \quad (10)$$

As the average power of the noise is

$$\bar{P}_N = 10^{-3} \text{W}, \quad (11)$$

the lowest S/N ratio for detecting the distorted Ricker wavelet sequence is

$$\frac{S}{N} = 10 \log \frac{\bar{P}_R}{\bar{P}_N} = 10 \log \frac{1.63 \times 10^{-4}}{10^{-3}} \approx -7.88 \text{ dB}. \quad (12)$$

This result demonstrates that the energy ratio between the Ricker wavelet sequence and the random noise is nearly 1:6.1, and hence, the capability of the method to detect a noisy signal. One may hope at least the same success when dealing with reflected signals obtained in seismic prospecting.

However, in spite of this excellent laboratory result, the level of noise mixed with the Ricker wavelet sequence does impinge on the chaotic behaviour of system. For example, if the noise level is too

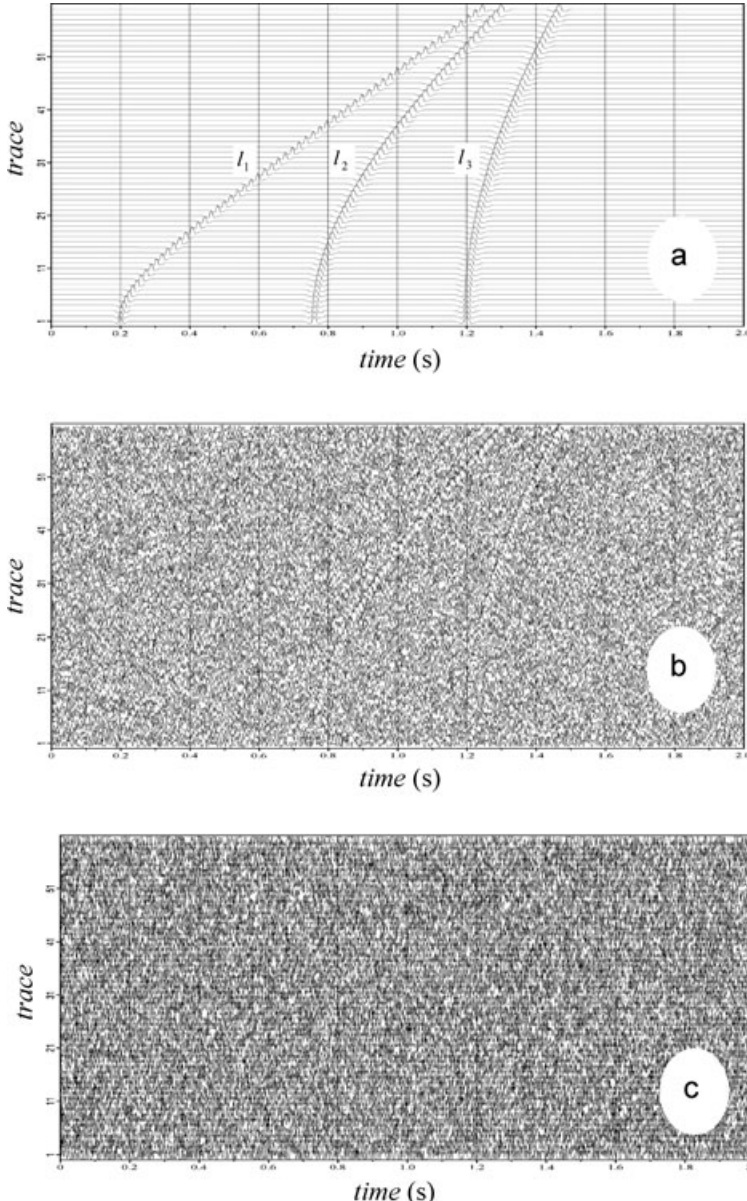


Figure 7. Record sections composed of 60 traces affected by three noise levels: $S/N = \infty$ (a), 0 dB (b) and -3 dB (c). In all cases, the synthetic seismograms were generated with a Ricker-type wavelet with decreasing frequency as the depth increases and neglecting anelastic attenuation with distance. Three reflecting layers are revealed: l_1 , l_2 and l_3 . In absence of noise the three reflection events are clearly visible, but when $S/N = 0$ dB only the second event and part of the third one can be seen with clarity and when $S/N = -3$ dB the three reflection events are invisible.

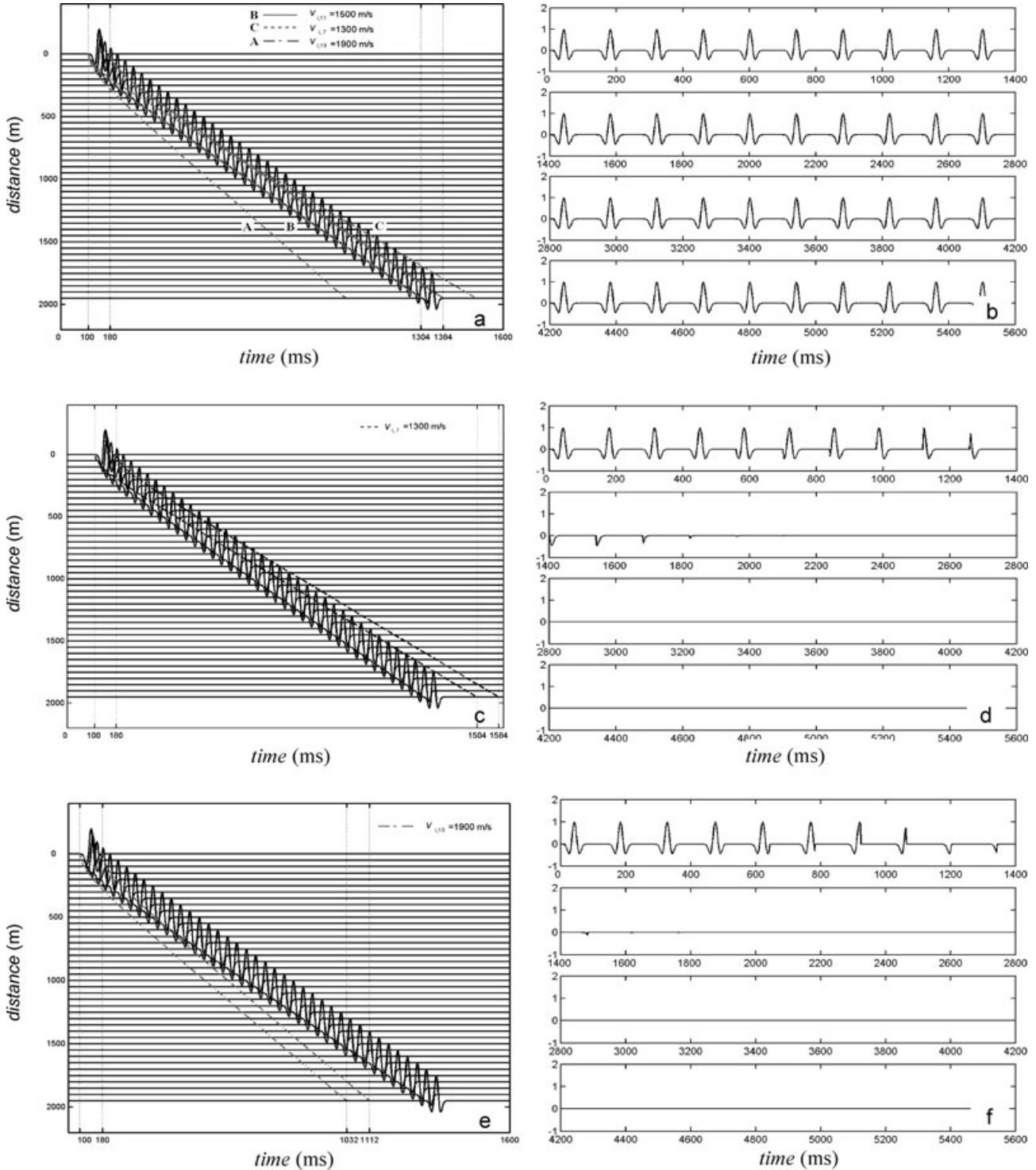


Figure 8. Free-of-noise synthetic common shot record revealing a seismic reflection from an elastic layer. Each arrival of energy is simulated by a Ricker-type wavelet of dominant frequency 25 Hz, which propagates with velocity of 1500 m s^{-1} . The offset (source–receiver distance) of the first channel is zero and the arrival time of the first onset is 100 ms. The receivers are equally spaced 50 m and the number of traces is 40. Theoretical arrival times for velocities 1900, 1500 and 1300 m s^{-1} are marked at different offsets by three straight (dash) lines A, B and C, respectively. On the right: Recovered seismic signal after applying the horizontal dynamic correction to the traces. The scanning interval on each wavelet is 80 ms and the time gap between adjacent wavelets is 60 ms. The i th wavelet corresponds to the wavelet of the i th channel. Central part: Similar common shot record and reflection event, but scanned with velocity 1300 m s^{-1} . On the right: Recovered seismic signal after applying the horizontal dynamic correction to the traces. Since the scanning velocity 1300 m s^{-1} is less than before, the intercepted onsets are not completely selected and supply distorted forms of decreasing amplitude with gradually smaller first negative troughs. Lower part: Similar common shot record and reflection event, but scanned with velocity 1900 m s^{-1} . On the right: Recovered seismic signal after applying the horizontal dynamic correction to the traces. Since the scanning velocity 1900 m s^{-1} is greater than before, the intercepted onsets are not completely selected and supply distorted forms of decreasing amplitude with gradually smaller second negative troughs.

Table 1. Data concerning the results plotted in Fig. 9: scanning velocity values, sampling arrival times and changes in the phase state of the oscillator system. The numbers of wavelets after scanning the same common shot record are also reported.

Scanning velocity V_{rms} (m s $^{-1}$)	Sampling times t_0 (s)	Phase state C, chaotic L, large-scale	No. of entire wavelets N	No. of truncated wavelets before the entire wavelets N_{before}	No. of truncated wavelets behind the entire wavelets N_{behind}
1000	0.4, 0.45, 0.5, 0.55	C, C, L, C	3, 4, 5, 0	2, 4, 0, 4	1, 1, 2, 0
1100	0.4, 0.45, 0.5, 0.55	C, L, L, C	3, 4, 6, 0	2, 5, 0, 4	2, 2, 3, 0
1200	0.4, 0.45, 0.5, 0.55	L, L, L, C	4, 5, 7, 0	2, 6, 0, 5	3, 3, 3, 0
1300	0.4, 0.45, 0.5, 0.55	L, L, L, C	6, 6, 8, 0	3, 7, 0, 7	3, 4, 5, 0
1400	0.4, 0.45, 0.5, 0.55	L, L, L, C	8, 9, 11, 0	4, 9, 0, 9	5, 6, 8, 0
1500	0.4, 0.45, 0.5, 0.55	L, L, L, C	14, 16, 18, 0	8, 12, 0, 18	6, 12, 15, 0
1600	0.4, 0.45, 0.5, 0.55	L, L, L, L	0, 0, 40, 11	21, 40, 0, 29	0, 0, 0, 0
1700	0.4, 0.45, 0.5, 0.55	C, C, L, L	0, 0, 18, 17	0, 21, 0, 14	0, 0, 19, 9
1800	0.4, 0.45, 0.5, 0.55	C, C, L, L	0, 0, 13, 11	0, 0, 0, 10	0, 0, 10, 9
1900	0.4, 0.45, 0.5, 0.55	C, C, L, L	0, 0, 10, 9	0, 0, 0, 9	0, 0, 8, 6
2000	0.4, 0.45, 0.5, 0.55	C, C, L, L	0, 0, 9, 7	0, 0, 0, 9	0, 0, 7, 5
2100	0.4, 0.45, 0.5, 0.55	C, C, L, L	0, 0, 9, 7	0, 0, 0, 8	0, 0, 5, 4
2200	0.4, 0.45, 0.5, 0.55	C, C, L, L	0, 0, 8, 6	0, 0, 0, 8	0, 0, 6, 4
2300	0.4, 0.45, 0.5, 0.55	C, C, L, L	0, 0, 8, 6	0, 0, 0, 7	0, 0, 5, 4
2400	0.4, 0.45, 0.5, 0.55	C, C, L, L	0, 0, 8, 6	0, 0, 0, 7	0, 0, 4, 3
2500	0.4, 0.45, 0.5, 0.55	C, C, L, L	0, 0, 7, 6	0, 0, 0, 7	0, 0, 5, 3
2600	0.4, 0.45, 0.5, 0.55	C, C, L, L	0, 0, 7, 5	0, 0, 0, 7	0, 0, 4, 3
2700	0.4, 0.45, 0.5, 0.55	C, C, L, L	0, 0, 7, 5	0, 0, 0, 7	0, 0, 4, 3
2800	0.4, 0.45, 0.5, 0.55	C, C, L, L	0, 0, 7, 5	0, 0, 0, 7	0, 0, 4, 3
2900	0.4, 0.45, 0.5, 0.55	C, C, L, L	0, 0, 7, 5	0, 0, 0, 6	0, 0, 4, 3
3000	0.4, 0.45, 0.5, 0.55	C, C, L, L	0, 0, 6, 5	0, 0, 0, 6	0, 0, 5, 3
3100	0.4, 0.45, 0.5, 0.55	C, C, L, L	0, 0, 6, 5	0, 0, 0, 6	0, 0, 4, 3
3200	0.4, 0.45, 0.5, 0.55	C, C, L, L	0, 0, 6, 5	0, 0, 0, 6	0, 0, 4, 3
3300	0.4, 0.45, 0.5, 0.55	C, C, L, L	0, 0, 6, 5	0, 0, 0, 6	0, 0, 4, 3
3400	0.4, 0.45, 0.5, 0.55	C, C, L, L	0, 0, 6, 5	0, 0, 0, 6	0, 0, 4, 3
3500	0.4, 0.45, 0.5, 0.55	C, C, L, L	0, 0, 6, 5	0, 0, 0, 6	0, 0, 4, 2
3600	0.4, 0.45, 0.5, 0.55	C, C, L, L	0, 0, 6, 5	0, 0, 0, 6	0, 0, 4, 2
3700	0.4, 0.45, 0.5, 0.55	C, C, L, L	0, 0, 6, 5	0, 0, 0, 6	0, 0, 4, 2
3800	0.4, 0.45, 0.5, 0.55	C, C, L, L	0, 0, 6, 5	0, 0, 0, 6	0, 0, 4, 2
3900	0.4, 0.45, 0.5, 0.55	C, C, L, L	0, 0, 6, 5	0, 0, 0, 6	0, 0, 3, 2

high, the mixed input signal might lead the chaotic oscillator having a state far from the periodic phase state and it would not be possible to ensure the existence of a weak periodic signal due to the low S/N threshold, which affects the capability of the system to detect weak signals. In other words, if the noise level is under the S/N threshold, then it is difficult to detect any weak signal.

3.1 On the noise threshold

There is an inherent difficulty in estimating the noise level and removing the background noise from the signal (Sheriff 1994), mainly because it is usually difficult to describe the quality of a seismic record by the S/N ratio, since both the strength and type of noise vary with time and for different reflected wavelets. S/N ratio is, therefore, only a rough quality criterion. The quality of a common shot record would be better defined by the S/N ratio as a function of the arrival time of a seismic reflection. However, the noise threshold can be determined via simulations with sinusoidal signals and it certainly varies as more complex signals are used. These experiments show that successful detection can be usually achieved if the S/N ratio is larger than 1:4. The proposed method is aimed at the detection of seismic events affected by strong background noise and it is desirable to develop an implementation for low S/N ratio. But how low may the S/N ratio drop?

Here we adopt the definition $S/N = 10 \log (S_w/N_n)$, where N_n is the average power of noise and S_w is the energy of the equivalent

seismic wavelet. In seismic prospecting of hydrocarbons it may occur that $S_w/N_n \approx 1$, and thus, $S/N \approx 0$ dB. We illustrate this topic using synthetic seismograms in three test cases: $S/N = \infty$ (absence of noise), 0 dB (1:1) and -3 dB (1:2). We do not show examples with higher noise level because in practice it is more difficult to identify events when S/N is less than -3 dB. Fig. 7 show synthetic common shot records composed of 60 traces with constant trace gap $\Delta x = 50$ m, simulated with a Ricker-type wavelet as signal reflected at different depths. Each one of these record sections reveals the existence of three events coming from reflecting layers l_1 , l_2 and l_3 at increasing depth, with wavelet dominant frequencies 35, 32 and 28 Hz, respectively. The arrival times are $t_0(l_1) = 0.175$ s, $t_0(l_2) = 0.727$ s and $t_0(l_3) = 1.162$ s, clearly readable on the free-of-noise waveforms (Fig. 7a). Despite the effect of the S/N ratio (∞ , 0 and -3 dB) on the three sections, at least the events reflected from the layers l_2 and l_3 can still be identified in Fig. 7(b). There is, however, little information about these events in Fig. 7(c), since their locations cannot be identified and their arrival times are impossible to read. The goal of this method is just the detection of events in an environment as noisy as that represented in Fig. 7(c).

3.2 On the nature of the noise

The non-linear dynamic system is strongly immune to the most frequently encountered kinds of noise in geophysics: white, red and off-white (this latter is a kind of random noise close to white). The

noise may likely not be white (non-Gaussian, atmospheric disturbances, wind-induced pressure changes, standing or non-standing ocean pressure-waves on coasts, isotropic ambient seismic noise, cultural noise) but coherent such as surface waves or multiple waves coupled to the target seismic signal. The chaotic oscillator method is, therefore, doubly limited by the level (threshold) and type (coherent, complex) of noise. In spite of the method's limitations and possibility of failure to detect the existence of a weak event,

we shall demonstrate that it is possible to discriminate signal versus noise with low S/N ratio (Sections 5 and 6).

4 CONSTRUCTING A PSEUDO-PERIODIC SEISMIC SIGNAL

With the purpose of giving a detailed view of the procedure that is going to be applied, we now refer to the transformation of a seismic

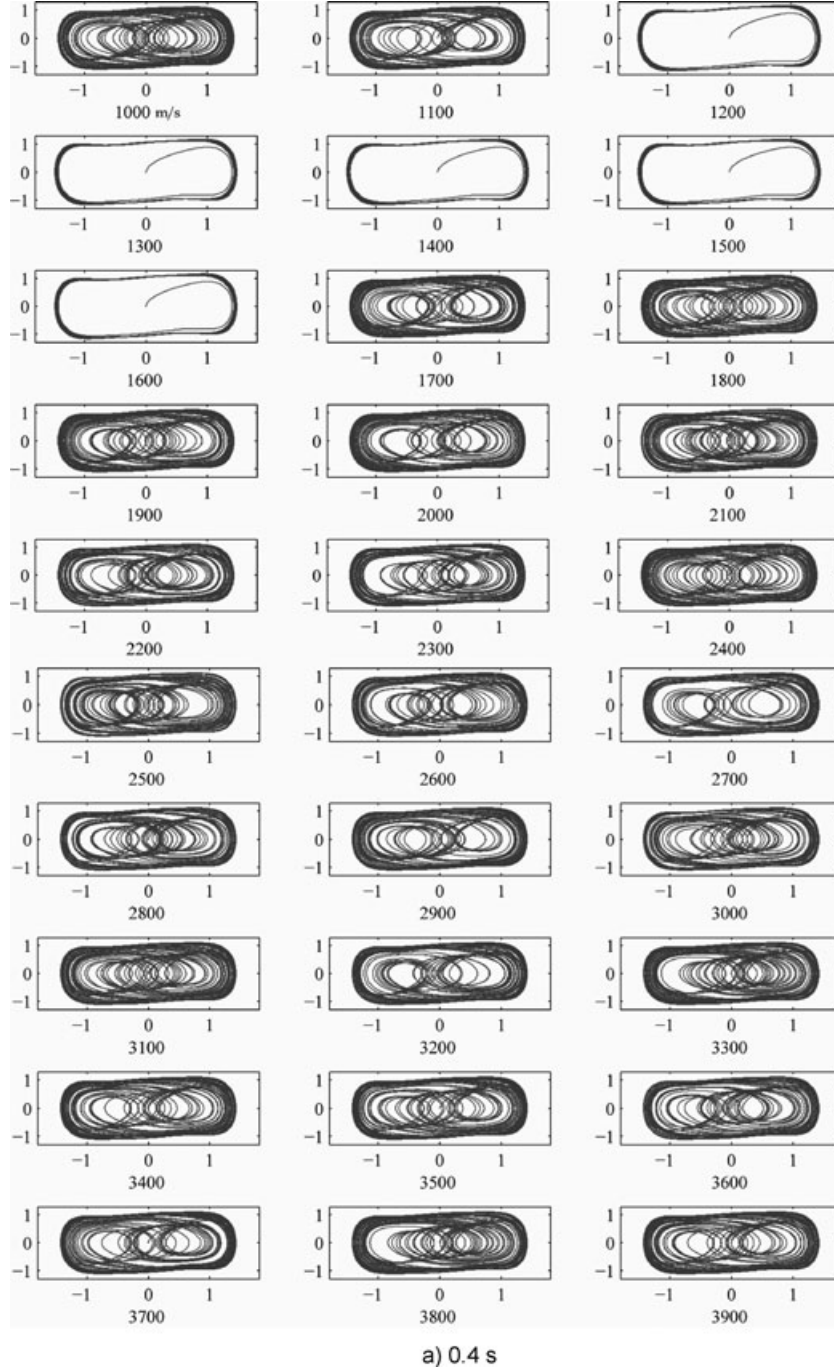


Figure 9. Changes in the orbits described in the phase space by a same oscillator excited by a hypothetical event whose arrival time and velocity are $t_0 = 0.5$ s and $V = 1600 \text{ m s}^{-1}$. Four scanning times were tried: (a) $t_0 = 0.40$ s; (b) $t_0 = 0.45$ s; (c) $t_0 = 0.50$ s; and (d) $t_0 = 0.55$ s. For each scanning time, up to 30 different configurations, corresponding to scanning velocities from 1000 to 3900 m s^{-1} at constant increments of 100 m s^{-1} , are displayed. Orbits depicting complex shapes image chaotic state of the dynamic system (C in Table 1), whereas simple orbits nearer to the elliptical shape image large-scale periodic state (L in Table 1).

event such as that recorded in practice into a signal that is easier to work with. An event in a common shot record represents a phase reflected from an impedance interface at a depth, which is detected by receivers at different offsets and times with reference to a common timescale. Due to this dependence upon location and time, the event is indeed a 2-D signal that must be converted into a time-series for detection by the chaotic oscillator method. The onsets reflected from the same interface in seismic prospecting have some similar features (basic shape, dominant frequency and phase of the wavelet) even though the noise is present. Thus, considering the hyperbolic equation describing the time-distance curve, all arrivals of the re-

flected seismic wavelets can be put on a single trace with a common reference time and the periodicity of the generated signal follows as a consequence of moveout at a particular scanning velocity. This operation, which requires the choice and testing of a set of arrival times and feasible scanning velocities, is called ‘horizontal dynamic correction’ (HDC) and leads to an artificial wave train, namely, a pseudo-periodic signal. A periodic signal must satisfy the following properties: first, it must be within the same interval in the time domain; second and third, it must have similarity and repeatability. After processing the signal by HDC the first condition is satisfied artificially; but the other properties, due to the scanning velocity,

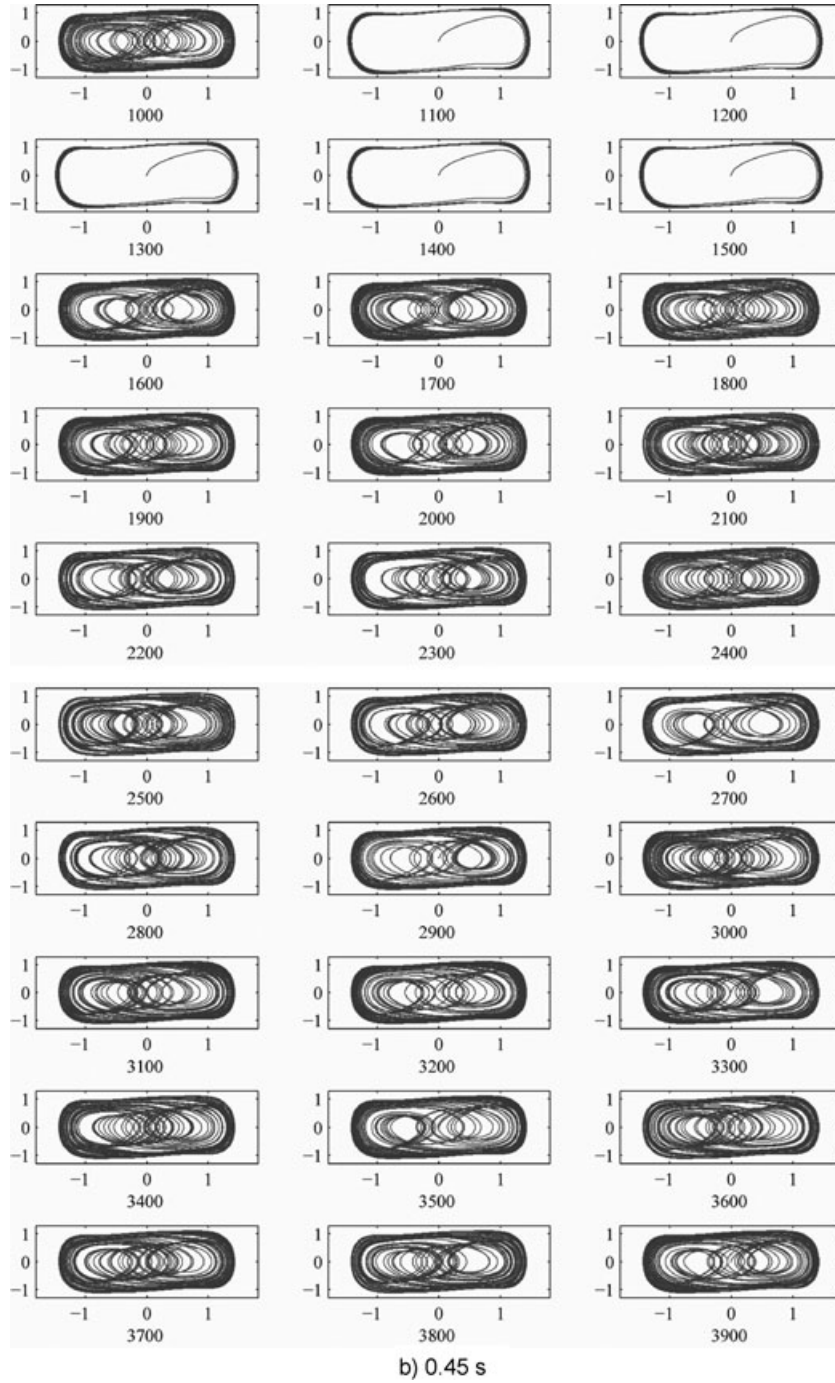


Figure 9. (Continued.)

usually cannot be ensured for the seismic wavelets coming from the same reflecting interface and arriving at different locations and therefore the artificially recovered time-series is actually a *nearly* periodic signal.

We illustrate the HDC process on a synthetic common shot record composed of 40 traces with a constant trace gap $\Delta x = 50$ m, where each energy arrival is simulated by a Ricker-type wavelet of dominant frequency $f_m = 25$ Hz, free-of-noise, under the constraints: first channel at zero-offset, arrival time of the first wavelet $t_0 = 100$ ms, velocity of the reflection event V_{rms} (simplified as V) = 1500 m s $^{-1}$. The anelastic attenuation with distance is neglected. The result is shown in Fig. 8(a). The hyperbolic equation describing

the time-distance curve is

$$t_{ik}^2 = t_{0i}^2 + \frac{x_k^2}{V_{ij}^2}, \quad (13)$$

where t is the traveltime of the seismic wave reflected from an interface to the geophones at surface, x is the offset, V is the simplified notation for V_{rms} , i is the event index, k is the trace index and j is the velocity index. In our case, $k = 0, 1, \dots, 39$; $j = 1, 2, \dots, J$, $J = 20$; $V_{i1} = 1000$ m s $^{-1}$; ΔV (velocity step) = 50 m s $^{-1}$. Given a velocity value, we can use eq. (13) to calculate the corresponding t_{ik} at different offsets x_k . To simplify the example, we only use three sample V_{rms} values for signal selection, namely, $V_{i,7} = 1300$ m s $^{-1}$,

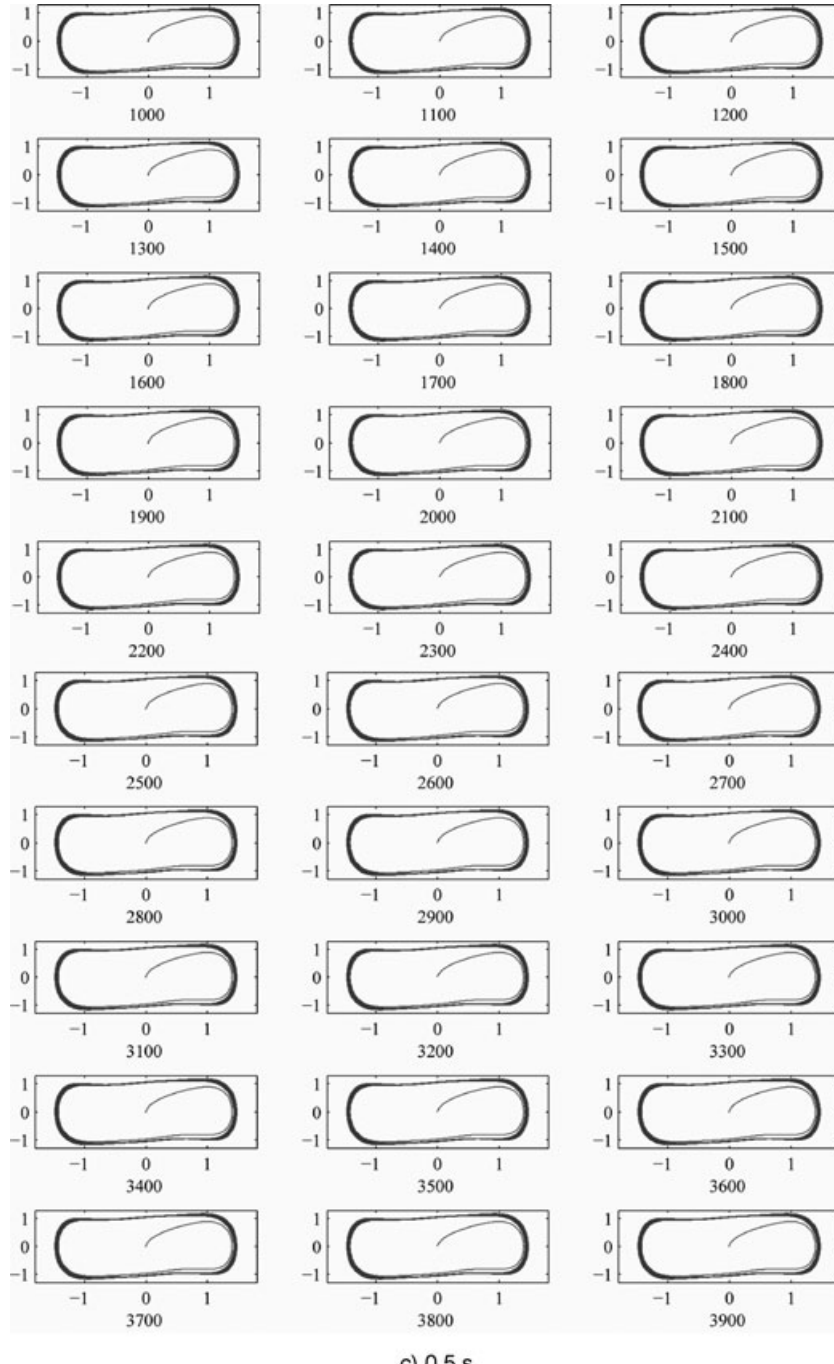


Figure 9. (Continued.)

$V_{i,11} = 1500 \text{ m s}^{-1}$ and $V_{i,19} = 1900 \text{ m s}^{-1}$. The result obtained by hyperbolic truncation with reference velocity $V_{i,11} = 1500 \text{ m s}^{-1}$ can be seen in Fig. 8(b). Analogously, the common shot records and the synthetic signals provided by HDC with scanning velocities $V_{i,7} = 1300$ and $V_{i,19} = 1900 \text{ m s}^{-1}$ are shown in Figs 8(c)–(f), respectively.

The results obtained by HDC with velocity $V_{i,11} = 1500 \text{ m s}^{-1}$ are almost perfect (Fig. 8b), as expected, but not the intercepted waveforms obtained with velocities $V_{i,7}$ and $V_{i,19}$ (Figs 8d and f), respectively.

which are not completely recovered from the original synthetic signal and are distorted traces where the first (Fig. 8d) and second (Fig. 8f) negative troughs are missing and the amplitudes decrease to a small spike. The final result obtained with velocity $V_{i,7}$ is a little better than the result achieved with $V_{i,19}$. After HDC processing with different V_{rms} values, the periodicity and repeatability characteristics of the new time-series have significant differences. Some of these time-series cannot lead the chaotic system to a large-scale periodic phase state and consequently they cannot be detected.

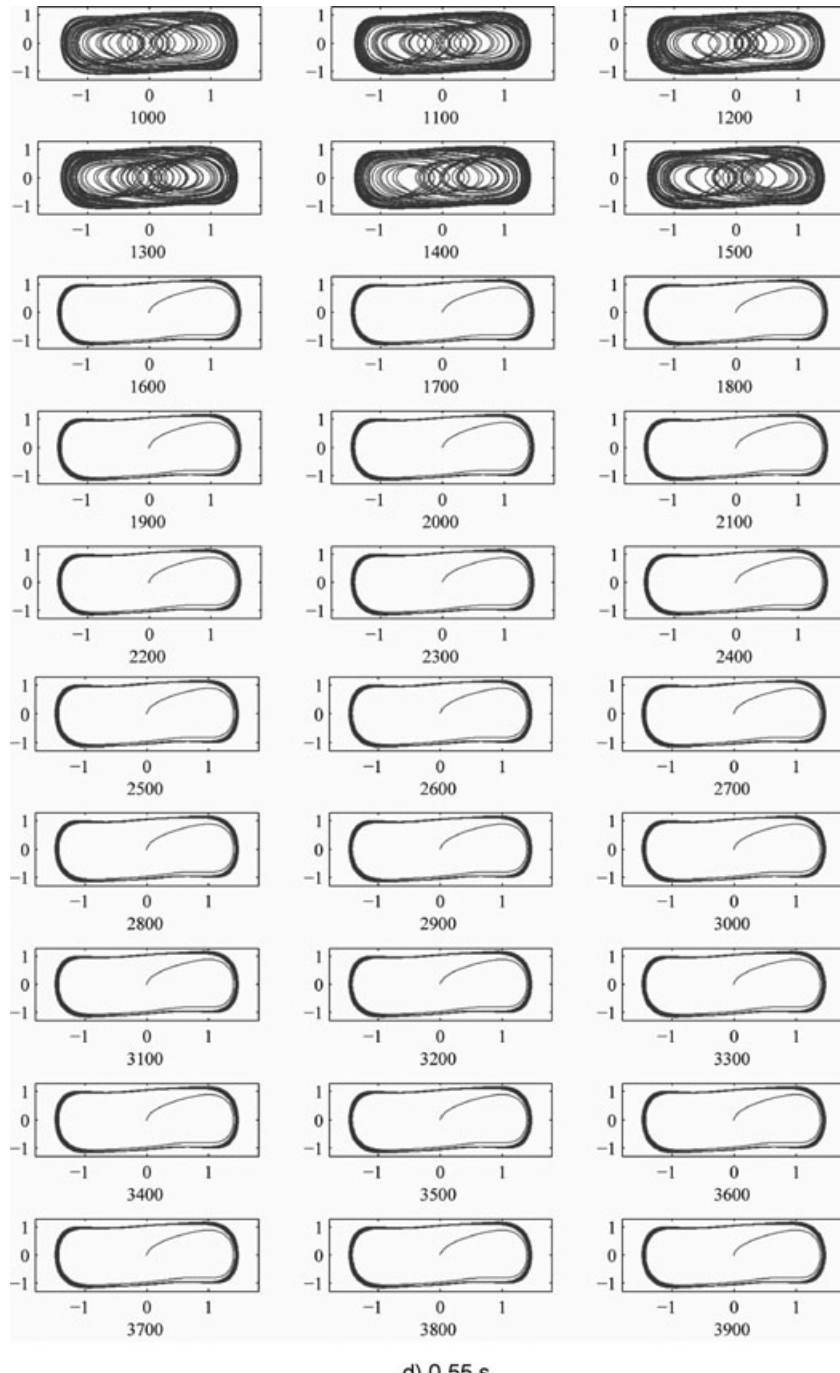


Figure 9. (Continued.)

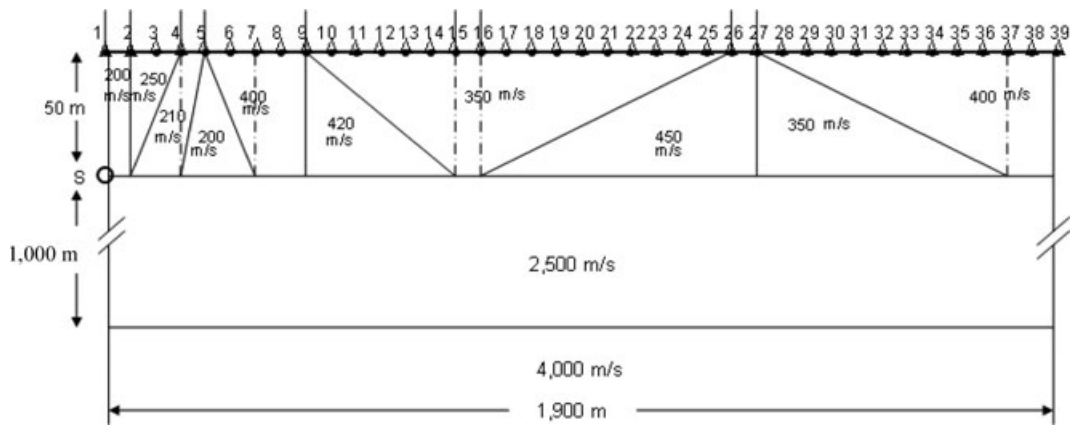


Figure 10. Layered model composed from top to bottom of a near-surface 50 m-thick low-velocity layer with complex geometry and laterally varying velocity between 200 and 450 m s^{-1} ; a 1000 m-thick layer with velocity 2500 m s^{-1} ; a semi-space with velocity 4000 m s^{-1} . The maximum horizontal offset is 1900 m. The medium is monitored by 39 equally spaced receivers installed at surface, which record the seismic energy coming from the source S.

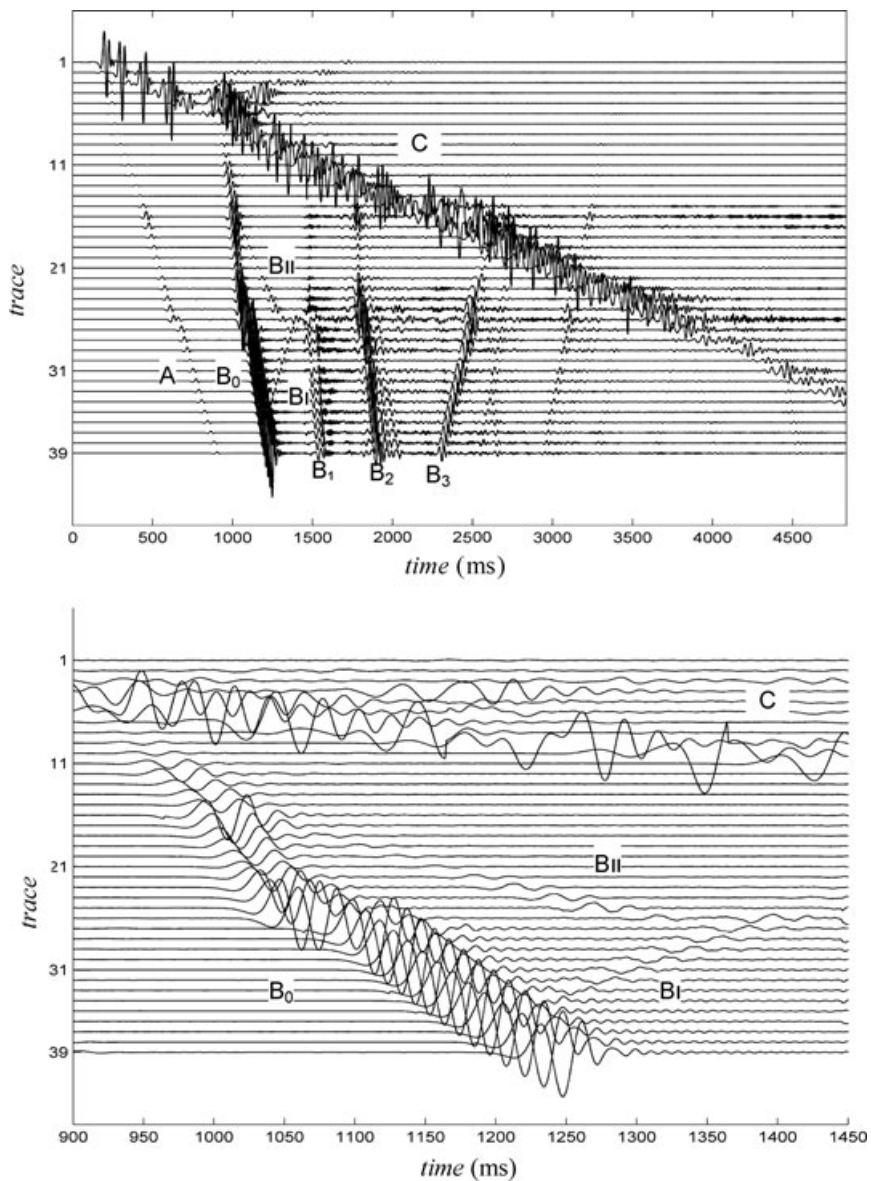


Figure 11. Synthetic record section constructed from the model and source S imaged in Fig. 10. Capital letters indicate observed seismic phases that are described in the text. Lower part: A zoom view of the waveforms, mainly of the B_0 wavefield.

4.1 Implementation

(1) It is very important to determine the first (V_{i1}) and last (V_{ij}) values of the scanning velocity V_{ij} . They are generally constrained by the velocities observed from good seismic records supplied by oil and gas exploration. In any case, a broad velocity range must be used for detection.

(2) In eq. (13), we have taken $\Delta V = 50 \text{ m s}^{-1}$ as the velocity step, but the increment in velocity $\Delta V(t_0)$ must be tested in any case. For example, for a deep reflecting layer ($t_0 > 3 \text{ s}$, t_0 being the traveltime of descent and return at zero-offset) ΔV may be larger than for other shallower reflecting layers ($t_0 \leq 3 \text{ s}$). However, an excessively large or small value of $\Delta V(t_0)$ would be inadmissible for further discrimination.

(3) Of course, the traveltimes corresponding to the arrivals from the shallowest reflecting layer ($t_{0i}\text{min}$) and the deepest reflecting layer ($t_{0i}\text{max}$) must be taken into account for implementation.

(4) The increment $\Delta t_0(t)$ of the initial time t_0 is a function of the reflection arrival time. The proper choice of this increment $\Delta t_0(t)$ must also be tested carefully. Δt_0 must be less than half of the minimum duration time DT_{\min} of a seismic wavelet to ensure that at least $t_0(i)$ and $t_0(i) + \Delta t_0$ fall into DT_{\min} ; otherwise, it is possible to skip over the event to be detected. If for instance $\Delta t_0 = 2 \text{ ms}$, the traveltime $t(x)$ calculated by eq. (13) could be inconsistent with the real arrival time of the event and the computation time would increase significantly. Nevertheless, once the characteristics of the seismic reflections are known during the course of the survey

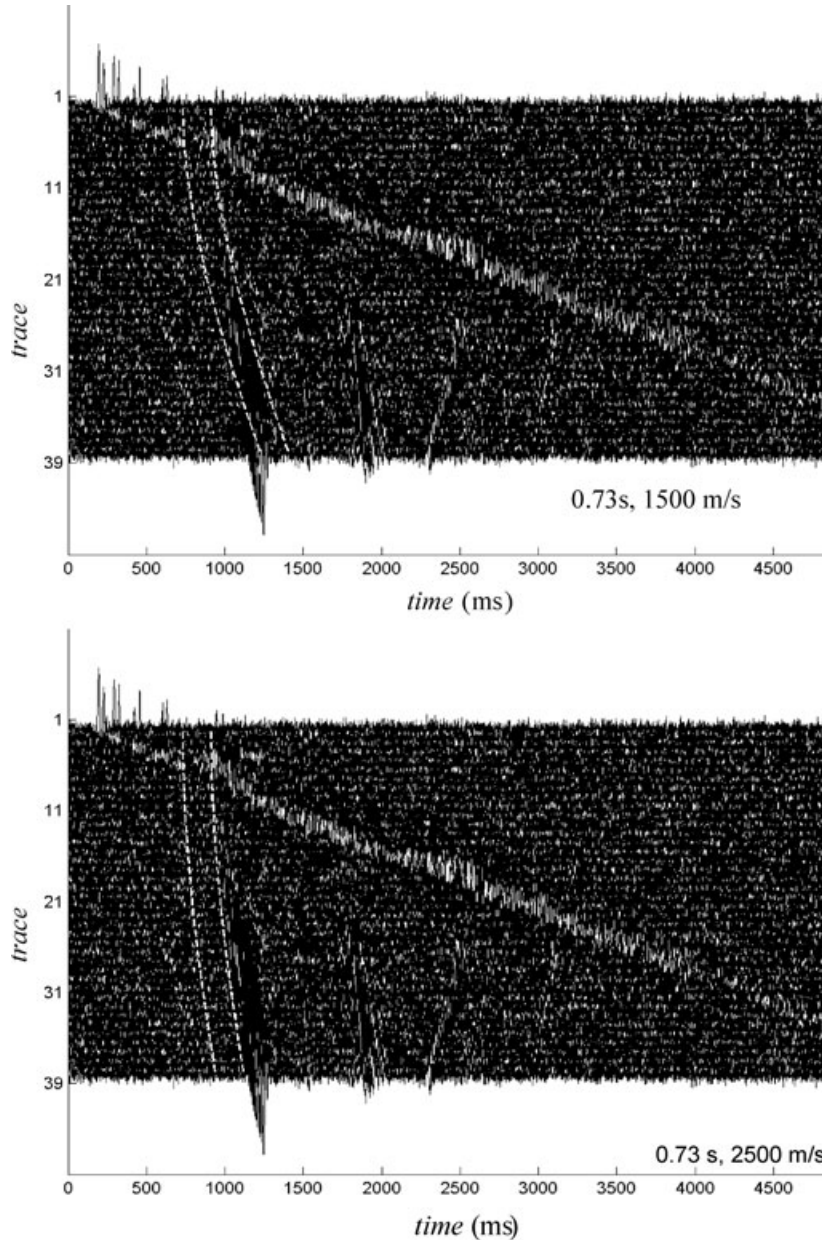


Figure 12. The common shot record is the same plotted in the upper part of Fig. 11, but contaminated by random noise. Distinct cutting bands of 180 ms, delimited by two time-offset curves (dash lines in white) computed from times 0.73 and 0.93 s and velocities 1500 and 2500 m s^{-1} , are outlined against the traces. The intercepted waveforms within these narrow bands lead to different 1-D wavelet sequences for chaotic detection analysis of the principal reflection event labelled as B_0 in Fig. 11.

of a basin, a relatively large value of Δt_0 can be used to save computing time.

(5) Moreover, the bigger the arrival time, the bigger the duration time of the seismic wavelet; consequently, it is desirable to conduct the analysis according to the seismic wavelet characters, such as dominant frequency, duration time, amplitude, etc., to select the wavelet with the shortest duration time.

(6) In practice, the HDC operation moves the wavelets on a single trace that is taken as input signal for detection by a chaotic oscillator; this process is automatically implemented and parameters, such as t_{0i} , V_{ij} , ΔV , k , etc., can be memorized for a further reconstruction of the seismic event after chaotic system detection.

5 EFFICIENCY TEST (1)

A common shot seismic record includes several events and random noise. The goal of the HDC processing is to obtain 1-D wavelet sequences for chaotic detection analysis and to search for possible events including their arrival times and transmission velocities. Assuming a noisy environment, in the following we focus our attention on some numerical experiments implemented with different trial values.

Let be a record section similar to the one displayed in Fig. 8(a), composed of 40 traces equally spaced 50 m and synthetically generated with a Ricker wavelet of dominant frequency $f_m = 30$ Hz. The

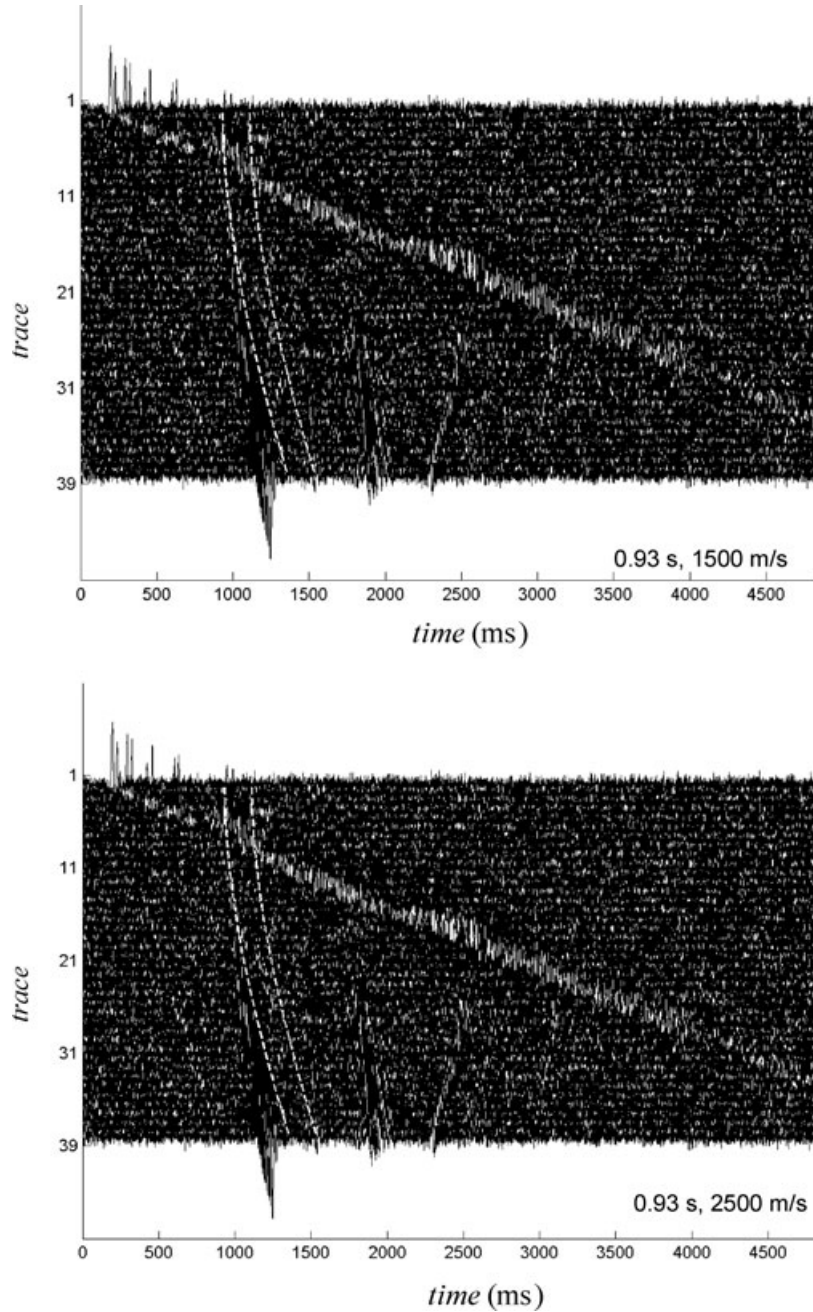


Figure 12. (Continued.)

record contains one seismic event whose arrival time and velocity are $t_0 = 0.5$ s and $V_{\text{rms}} = 1600 \text{ m s}^{-1}$, respectively. Random noise is initially present in all traces, with the S/N ratio near -3.7 dB. Without *a priori* information we have selected for sampling four sampling t_0 -values for data processing, $0.40, 0.45, 0.50$ and 0.55 s, and thirty scanning velocities, from 1000 to 3900 m s^{-1} at constant increments of 100 m s^{-1} . Next, for each time t_0 , we have processed up to 30 distinct configurations (the number of trial velocities) by the

chaotic detection method. Parameters for computation (sampling arrival times, scanning velocities, etc.) are given in Table 1. In this same table we report the number of entire and truncated wavelets that form each 1-D wavelet sequence. The results obtained after processing 120 (4×30) pseudo-periodic signals, i.e. the changes in the orbits described by the same chaotic oscillator (eq. 4) in the phase space, indicated in Table 1 for every sampling time, are plotted in Fig. 9. These results allow us to make the following observations:

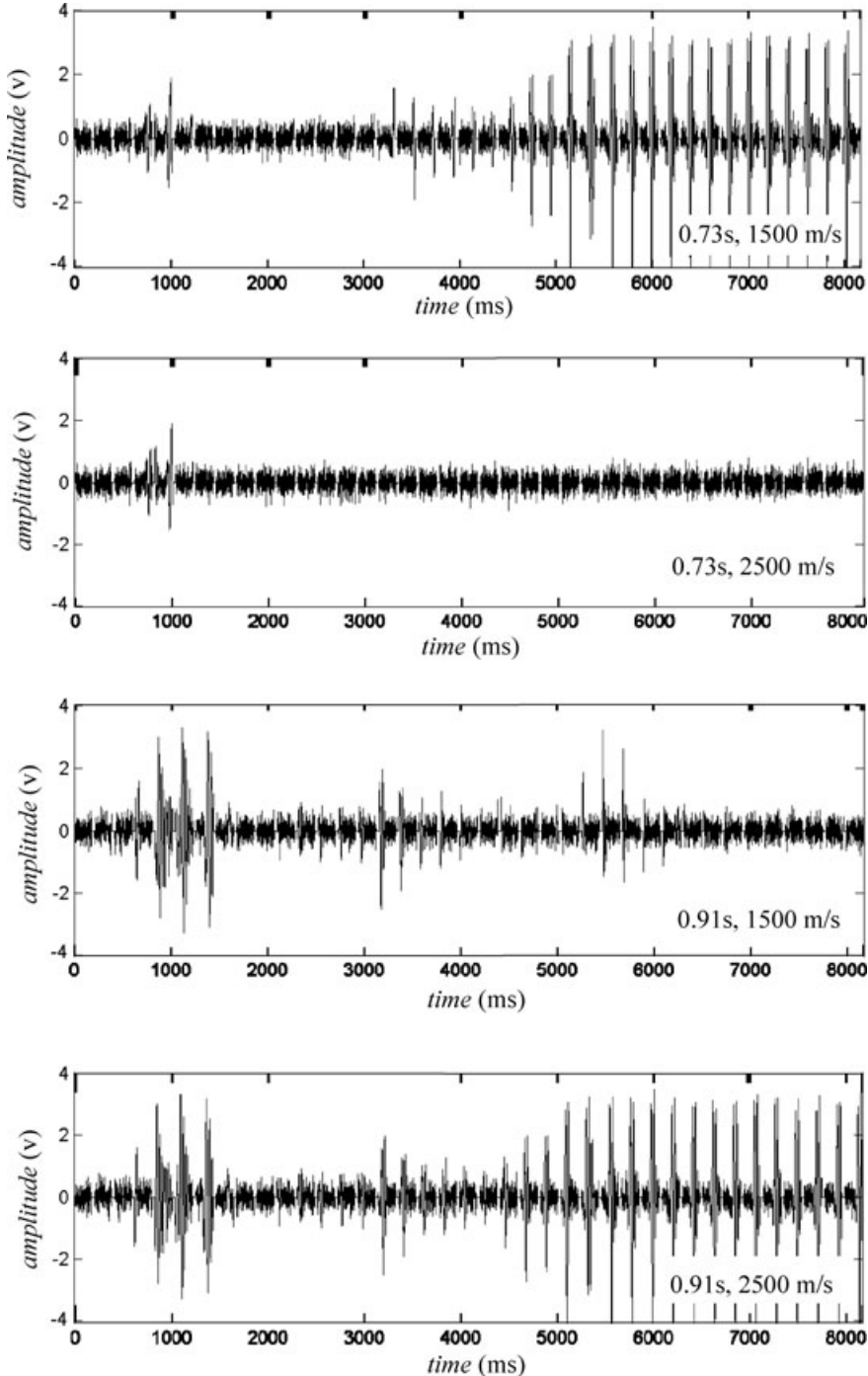


Figure 13. Examples of wavelet sequences recovered by cuts of waveforms within narrow bands of 180 ms (Fig. 12), identified by the arrival times $0.73, 0.91, 0.93, 0.95$ s and scanning velocities 1500 and 2500 m s^{-1} used for simulation. In all cases, the synthetic seismograms correspond to the tested reflection event labelled as B_0 in Fig. 11. Since the time window spans 180 ms, the time between adjacent wavelets is 30 ms and the number of recording channels is 39 , the seismograms go beyond 8000 ms.

(1) Given a time t_0 , the scanning velocity that leads the oscillator system to a large-scale periodic phase state is not unique, but a set of velocities, i.e. an information segment. This favourable result permits to understand that an event is present in the signal when a scanning interval makes the system reach a periodic phase state.

(2) For the smallest sampling time $t_0 = 0.40$ s and velocity $1200 \leq V_{\text{rms}} \leq 1600 \text{ m s}^{-1}$ the system reaches a large-scale periodic phase state; out of this interval the system is in chaotic state (Fig. 9a). For the largest sampling time $t_0 = 0.55$ s and velocity $V_{\text{rms}} < 1600 \text{ m s}^{-1}$ the chaotic state is the feature of the system; over this velocity value, $V_{\text{rms}} \geq 1600 \text{ m s}^{-1}$, the system exhibits a large-scale periodic phase state (Fig. 9d). For intermediate time $t_0 = 0.45$ s and

almost any velocity value the system is in chaotic state, except for the interval $1100 \leq V_{\text{rms}} \leq 1600 \text{ m s}^{-1}$ wherein the system reaches a large-scale periodic phase state (Fig. 9b). Finally, in the case of $t_0 = 0.50$ s and for any scanning velocity $1000 \leq V_{\text{rms}} \leq 3900 \text{ m s}^{-1}$ the system is always in a large-scale periodic phase state (Fig. 9c).

(3) The propagation velocity of the event is constrained by the maximum number of entire wavelets simulating the seismic signal, which in our example is 40 for arrival time $t_0 = 0.5$ s and velocity $V_{\text{rms}} = 1600 \text{ m s}^{-1}$, as expected (Table 1). These observations confirm both the arrival time and the rms velocity of the event and demonstrate the efficient detection of a weak seismic signal using a chaotic oscillator.

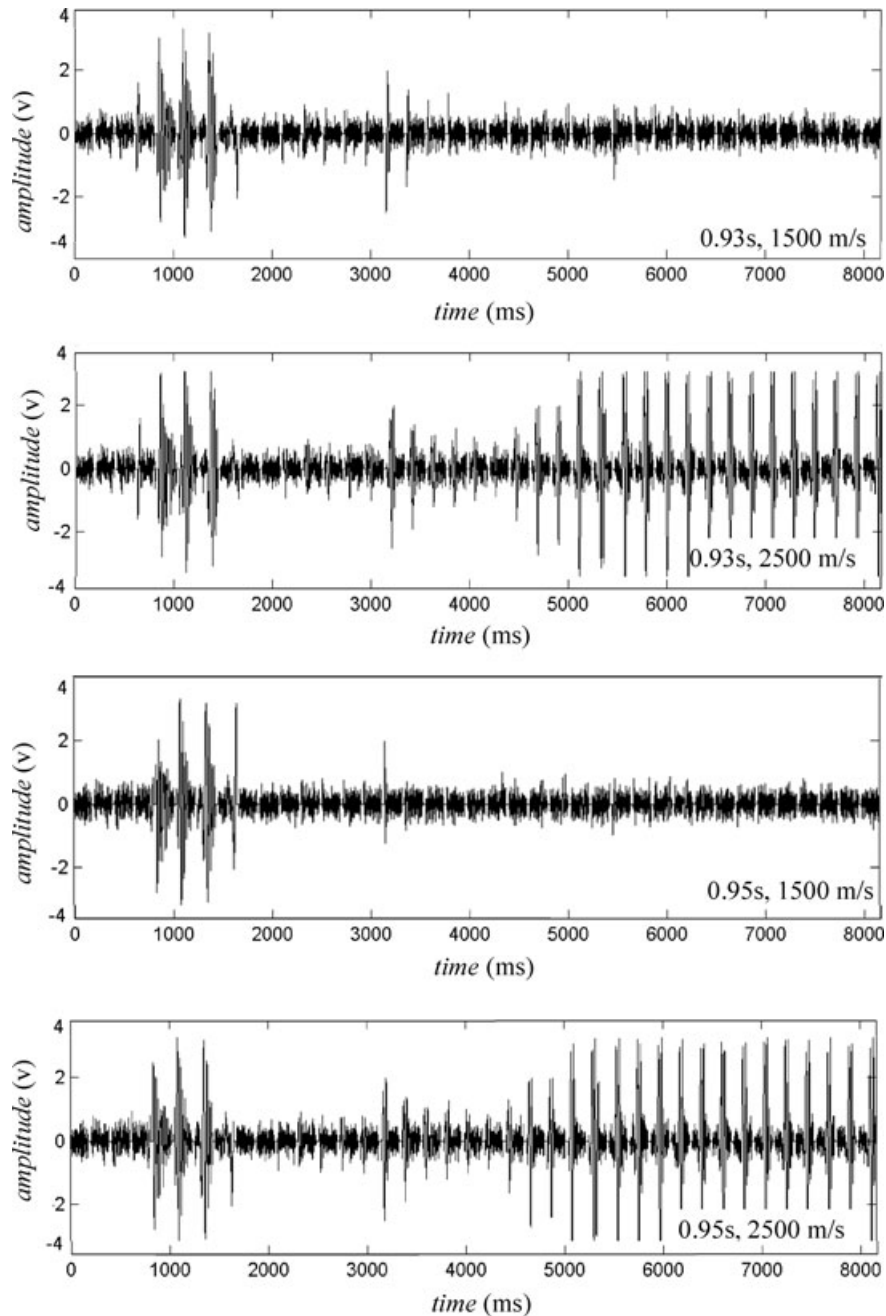


Figure 13. (Continued.)

6 EFFICIENCY TEST (2): FUNDAMENTAL WEAKNESS OF THE HDC TECHNIQUE

This weakness has its origin in the use of a particular scanning velocity when the transmission velocity of the seismic event can be

highly variable. Errors affecting the periodicity of the reconstructed signal would be due to smearing effects along seismic rays propagating for instance across a near-surface sedimentary layer with laterally varying seismic velocity. In the presence of this layer the periodicity of the signal could well be destroyed. In practice, several scanning velocities should be simulated, i.e. different sampling

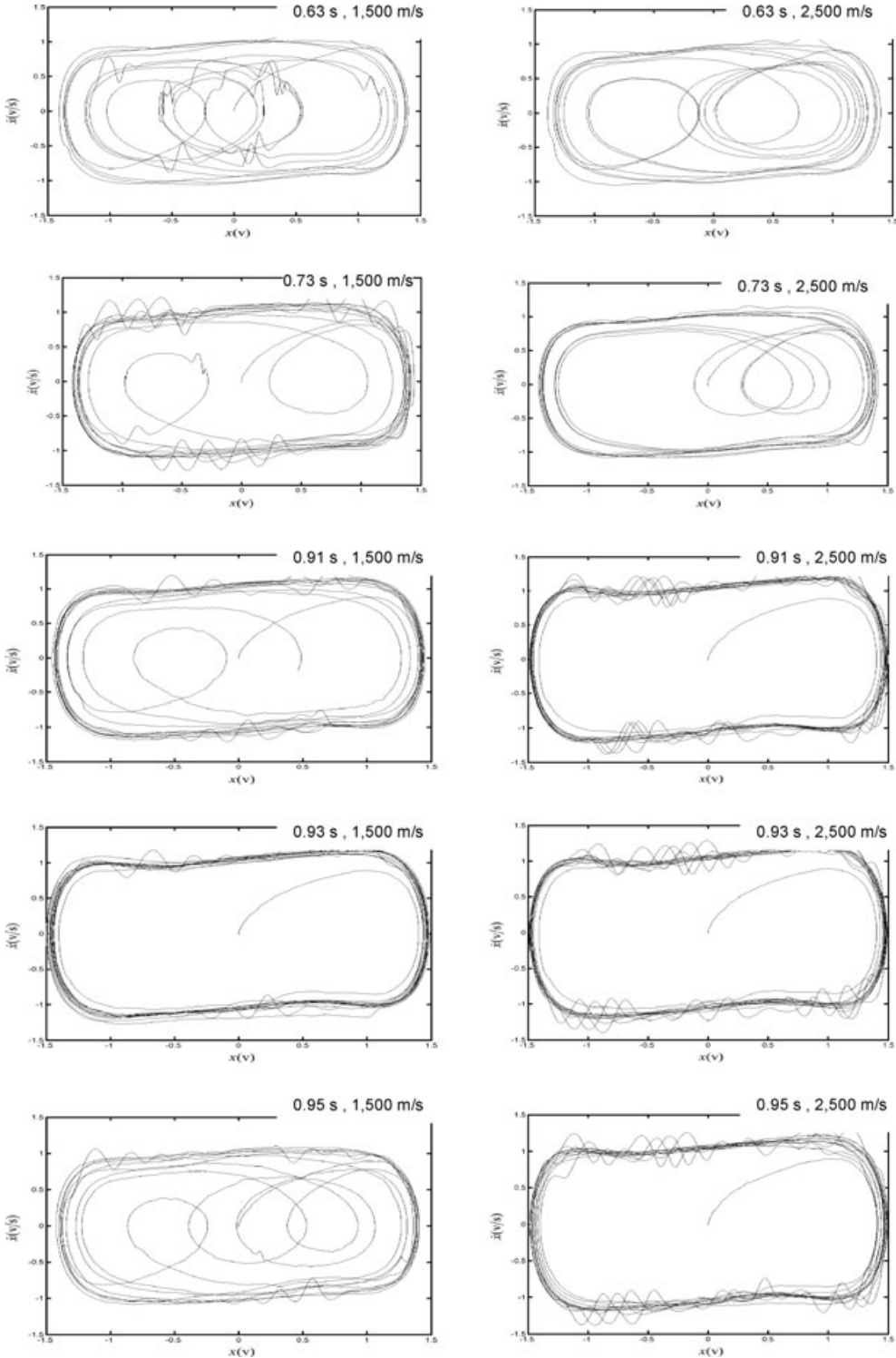


Figure 14. Orbits described by a same oscillator system (eq. 4) in the phase space when excited by the seismic signals plotted in Fig. 13. Combinations of arrival times 0.63, 0.73, 0.91, 0.93, 0.95 s and scanning velocities 1500 and 2500 m s⁻¹ permitting the identification of cutting bands (Fig. 12) and signals (Fig. 13), are used for labelling distinct configurations.

velocity values as consequence of the non-constant velocity of the event across such a layer. In this section, we explore this sensitivity issue affecting the possible fundamental weakness of the proposed technique searching for the effect caused by near-surface lateral velocity variation on the periodicity of the seismic signal recovered after using an optional scanning velocity.

With this goal we designed a numerical experiment under the assumption of a near-surface 50 m-thick low-velocity layer with complex geometry and laterally varying velocity between 200 and 450 m s⁻¹. This structure overlies other 1000 m-thick horizontal layer with velocity 2500 m s⁻¹, which lies on a semi-space with velocity 4000 m s⁻¹ (critical angle $\sim 38.7^\circ$). The maximum horizontal offset is 1900 m. Both the geometry and velocities of the weathered layer model are imaged in Fig. 10. For wave field computation the seismic source is supposed to be at the bottom of the

shallow layer at zero-offset and the energy recorded by 39 channels equally spaced 50 m, as many as virtual receivers on surface (Fig. 10). The synthetic common shot record was generated using a Ricker wavelet of dominant frequency $f_m = 35$ Hz and then solving the wave equation by finite differences at time step $\Delta t = 1$ ms. Fig. 11 (upper part) shows the section composed of waveforms more or less influenced by the complex geometry and laterally varying velocity of the top layer. The A-type arrivals (computed arrival time $t_0 = 0.413$ s) correspond to critical refractions along the bottom of the shallow layer and include refracted waves that can be linearly correlated. As for B-type arrivals, the B₀-event ($t_0 = 0.951$ s) is identified as the reflected phase from the deep interface (at depth 1050 m). One may distinguish three sets of traces, namely, 7 to 15th, 16 to 26th and 27 to 39th; the two firsts are a bit far from the hyperbolic branch of the theoretical time-offset curve due to the

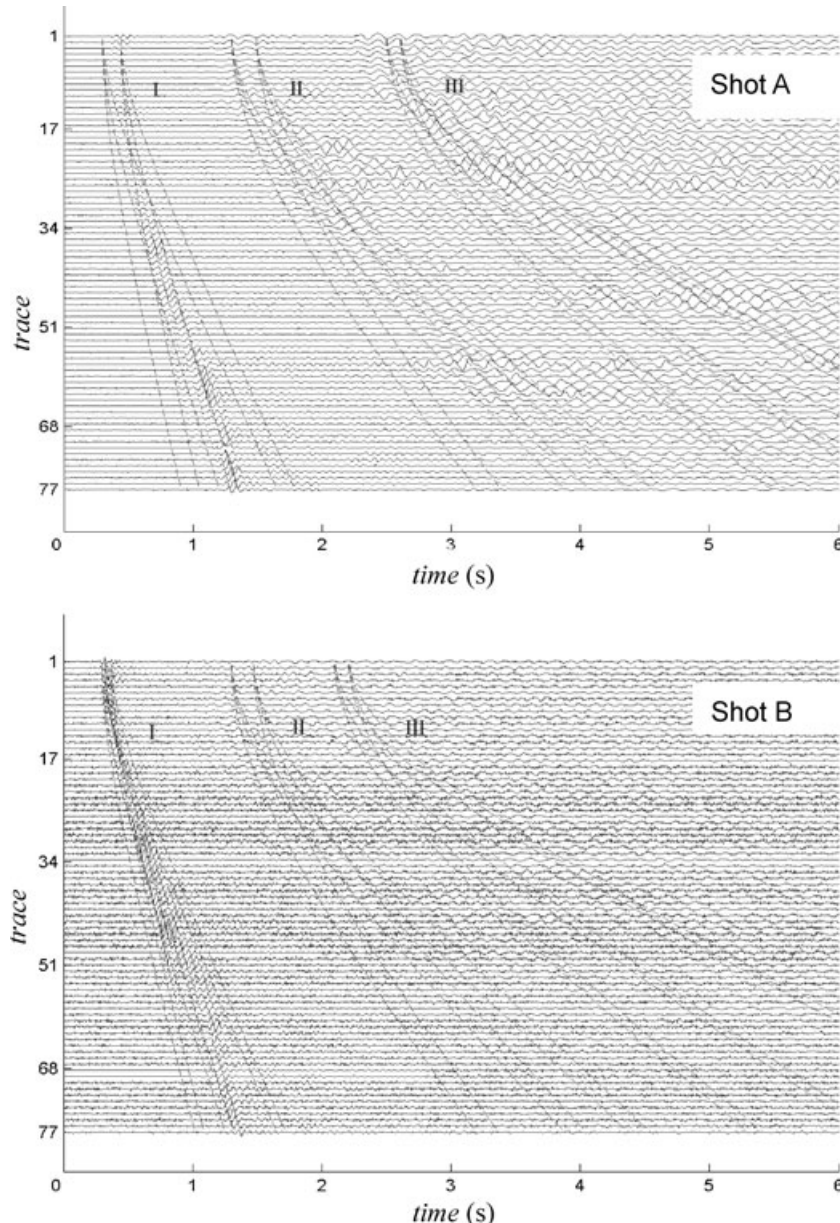


Figure 15. Seismic records composed by 77 traces with a trace gap of 40 m obtained from two shots A (upper part) and B (lower part) during the seismic exploration of a basin in China. Both records show three possible reflection events (marked as I, II and III) that in the case of shot B are contaminated by a higher noise level. Dashed lines represent hypothetical arrivals of seismic phases propagating with different trial velocities from different interfaces.

influence of the near surface layer, whereas the third set approaches the hyperbolic form (see enlarged section in Fig. 11, lower part). BI and BII are short-path phases first reflected from the deep interface and then refracted along the bottom of the low-velocity layer. B₁, B₂ and the late B₃ field are multiples, i.e. waves successively reflected at the bottom and top of the shallow layer. The C-type arrivals ($t_0 = 0.148$ s) are wave trains propagating from the source to the receivers across the weathered layer (Fig. 11, lower part).

Random noise (variance $\sigma^2 = 0.1$) is added *ab initio* to all traces to simulate a noisy environment, with the S/N ratio near -3.7 dB (Fig. 12). To process the synthetic record and particularly the B₀ field without *a priori* information, we deliberately selected a broad range of scanning velocities, from 1000 to 3900 m s⁻¹ at constant increments of 50 m s⁻¹ and arrival times 0.63, 0.73, 0.91, 0.93, 0.95, 1.13 and 1.23 s, because the reading of arrival time on the record is near $t_0 \approx 0.9$ s (Fig. 11, lower part). Fig. 12 shows several cutting (scanning) bands of traces (Fig. 11, upper part), all constrained within a same time window of 180 ms and delimited by pairs of time-offset curves calculated for hyperbolic truncation (eq. 13) from combinations of times 0.73 and 0.93 s and velocities 1500 and 2500 m s⁻¹.

Owing to the great amount of 1-D wavelet sequences obtained after applying the horizontal dynamic correction on the traces, i.e. by hyperbolic truncation of synthetic waveforms (eq. 13) using different arrival times and many optional scanning velocities (up to 59), we only show a few examples of recovered seismic signals for times 0.73, 0.91, 0.93, 0.95 s and velocities 1500 and 2500 m s⁻¹. The results based on the intercepted waveforms displayed in Fig. 13 allow us to estimate the effect caused by lateral velocity variation on the periodicity of the reconstructed signal, and therefore, to give a sound response to the problem initially posed. The best results for preliminary discrimination come from the combina-

tions of times 0.91, 0.93, 0.95 s and scanning velocities 1500–2500 m s⁻¹ that supply pseudo-periodic signals. The final discrimination is due to the excitation of the oscillator system (eq. 4) and observation of the orbits described in the phase space. The pairs of sampling values 0.63, 0.73, 0.91, 0.93, 0.95 s and 1500 m s⁻¹, and therefore, the velocity 1500 m s⁻¹, can be discarded as feasible solutions as they lead to chaotic orbits (Fig. 14). However, the orbits obtained for velocity 2500 m s⁻¹ and time 0.91–0.95 s lead the system to a stable periodic phase state (Fig. 14), and thus, these values seem to be the most suitable results provided by the analysis. This proves that the HDC technique is able enough to detect the main reflection event picked up from the record section despite the strong contrasts of seismic velocity and noise level affecting the data.

Checking the weakness of the technique by similar tests conducted with different sedimentary-cover velocities and thicknesses yield the same conclusion, since the respective effects are merely a time-shift of the reflected onsets crossing the top layer, which does not introduce an important bias on the wavelet sequence. The case of dipping layer could be analysed analogously. Consequently, the numerical experiment developed is a conclusive analysis about the power and reliability of the technique.

7 A CASE STUDY WITH REAL DATA

We now carry out an application to real data to provide a convincing argument for the usefulness of the method. Given this task, we consider two common shot seismic records acquired during the course of a seismic survey of a basin in China using explosive-source technology. Each record is composed of 77 traces equally spaced and digitized at a sampling rate of 1000 sps. Two different shots, A and B, were fired at distance of some 800 m from the

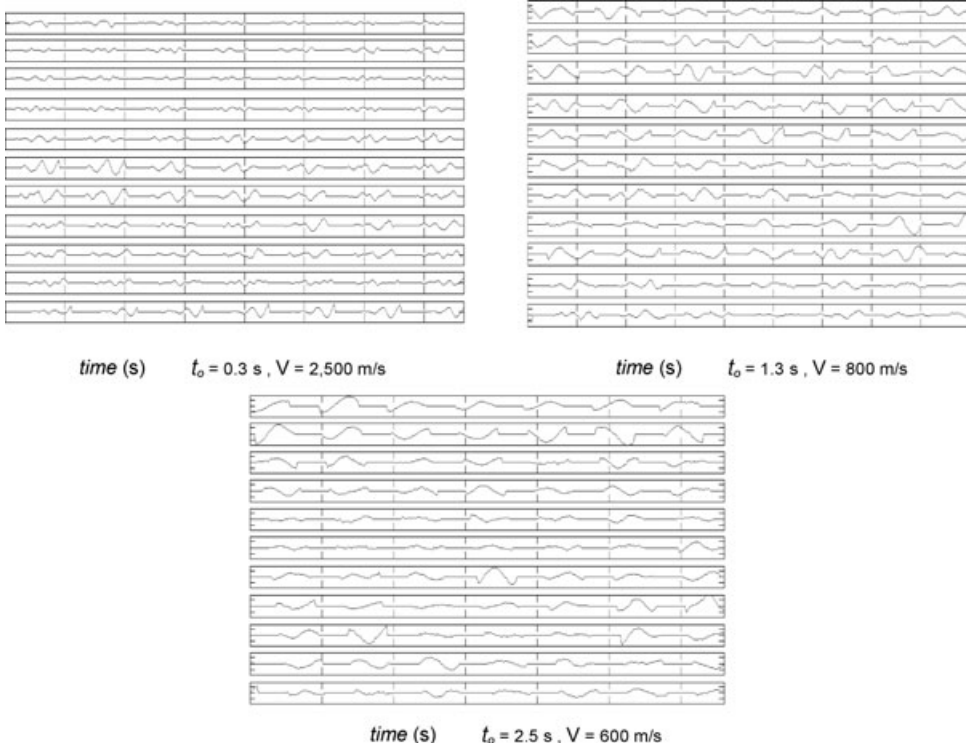


Figure 16. Wavelet sequences after applying the horizontal dynamic correction to the traces shown in Fig. 15 (upper part). As control times and velocities were taken: (a) $t_0 = 0.3$ s, $V = 2500$ m s⁻¹; (b) $t_0 = 1.3$ s, $V = 800$ m s⁻¹; and (c) $t_0 = 2.5$ s, $V = 600$ m s⁻¹.

nearest station and recorded with an average trace gap of 40 m along the recording line. Each shot consisted of a hole drilled at very shallow depth and loaded with a charge of about 30 kg of explosive. Both the information collected from the record section of shot A (Fig. 15, upper part) and the record section of shot B (Fig. 15,

lower part) show three possible reflection events, labelled I, II and III, although in the second case affected by a higher noise level that partially hides them and makes their identification and further correlation difficult, above all regarding the most delayed energy arrivals (II and III) that clearly appear buried by noise.

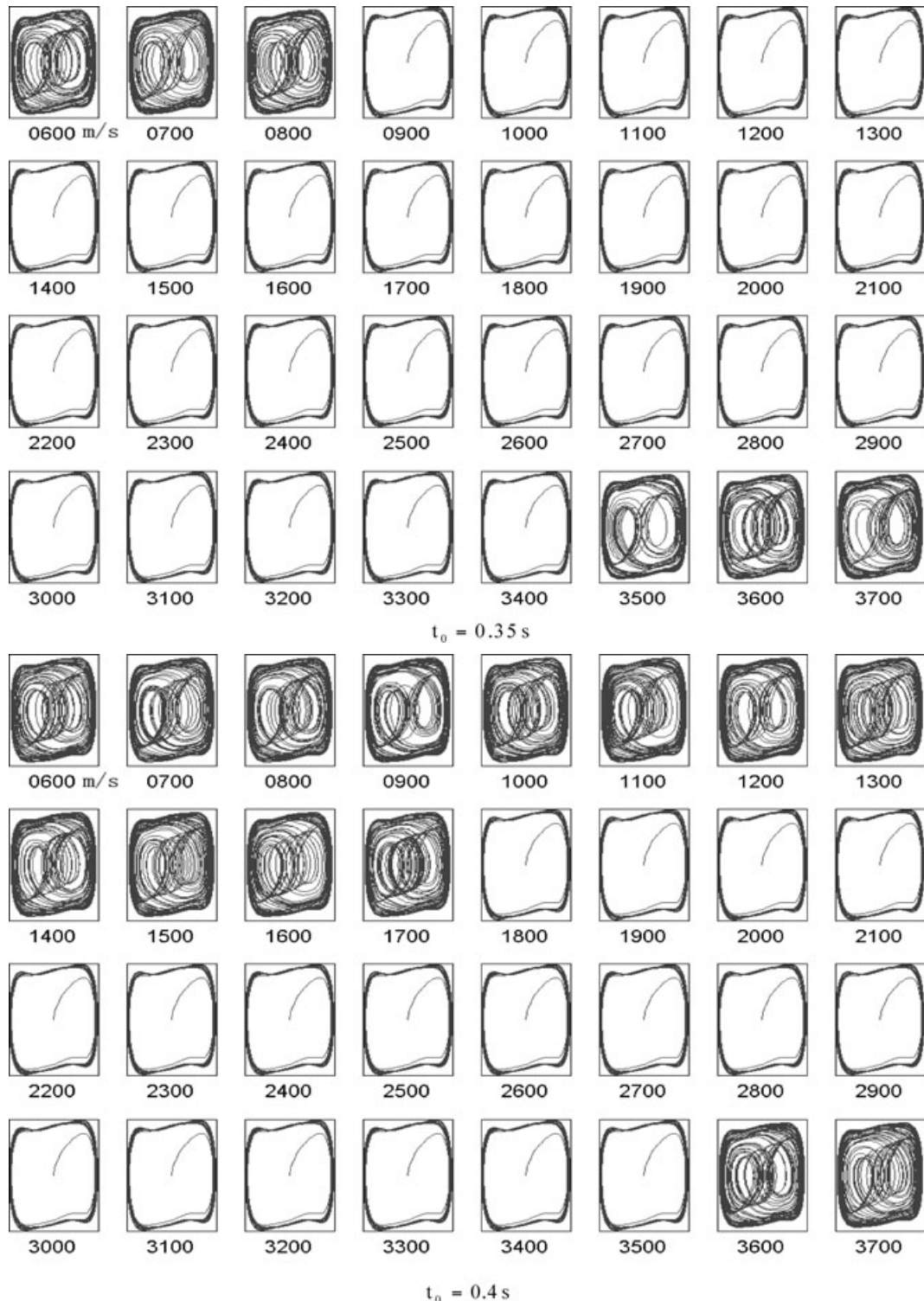


Figure 17. Orbits described by a same oscillator system (eq. 4) in the phase space showing different configurations obtained from 32 scanning velocities (from 600 to 3700 m s⁻¹ and from 500 to 3600 m s⁻¹) and various arrival times (0.35, 0.40, 0.45, 1.25, 1.35, 1.50, 2.40, 2.45 and 2.55 s), with reference to possible reflection seismic events recorded after shot A (Fig. 15, upper part).

The three events exhibit arrival times and apparent velocities ranging between 0.1–5.0 s and 600–3700 m s⁻¹; therefore, only values belonging to these intervals were chosen to process the common shot records displayed in Fig. 15. For all energy arrivals the horizontal dynamic correction of the seismic wavelets is performed by hyperbolic truncation of the traces corresponding to the three

events using scanning velocities from 600 to 3700 m s⁻¹ at constant increments of 100 m s⁻¹, except for some arrivals type III from shot A for that the scanning velocities were 500–3600 m s⁻¹. The theoretical time-offset curves for truncation were previously calculated by eq. (13) and some of them are represented by dashed lines in Fig. 15. Since the duration of the onsets is not always the same,

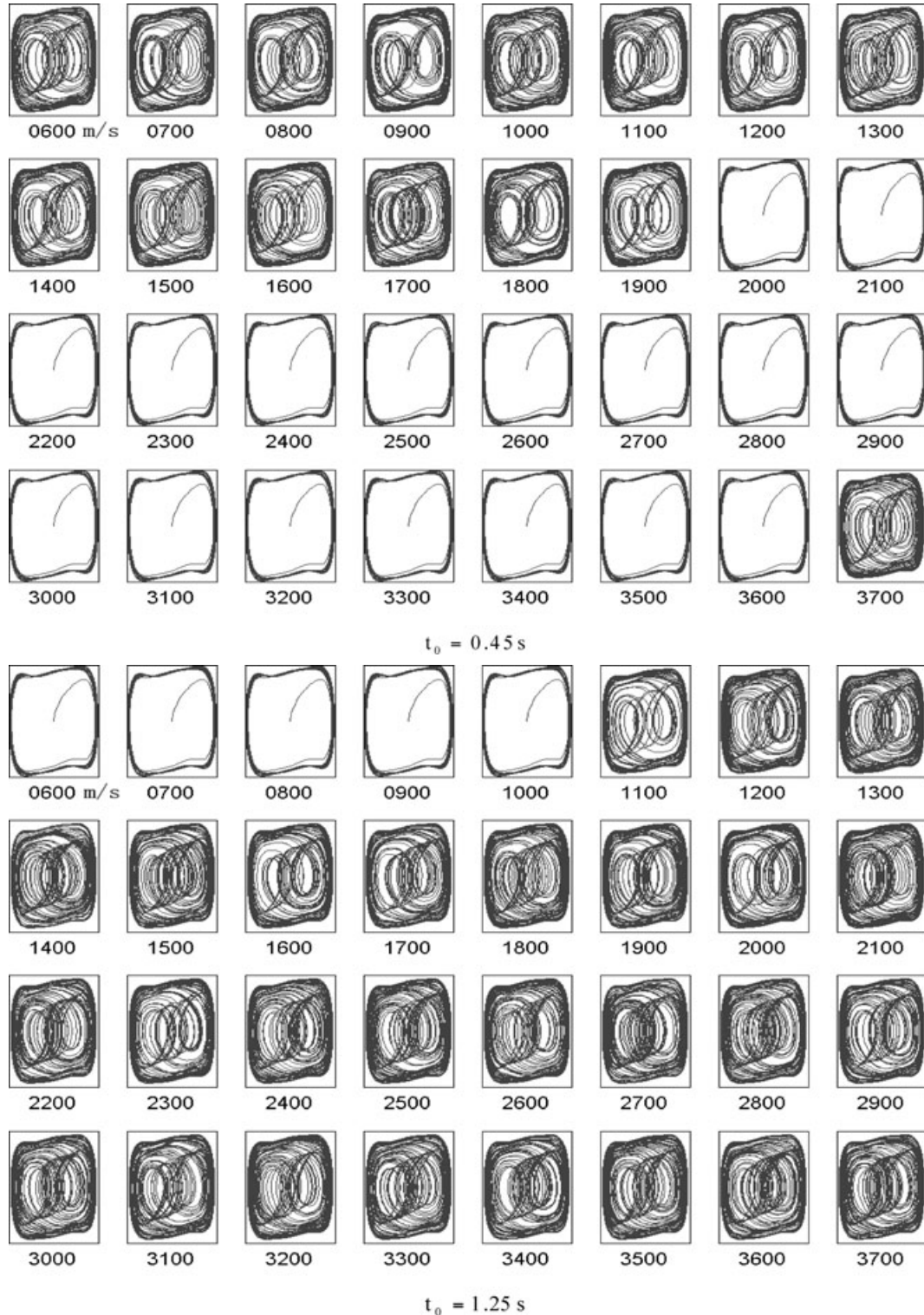


Figure 17. (Continued.)

we have taken time windows of 140, 190 and 110 ms for wavelets classified as I, II and III, respectively. Also, we have tried various sampling arrival times t_0 for construction of the respective input signals, namely, 0.30, 0.35, 0.40, 0.45, 0.50 s for waves labelled as I; 1.10, 1.15, 1.20, 1.25, 1.30, 1.35, 1.50 s for waves labelled as II; 2.40, 2.45, 2.50, 2.55 s for waves labelled as III. Given that the information to be processed is indeed abundant (we have in-

vestigated 1024 configurations from 16 time values \times 32 scanning velocity values \times 2 records) we only provide some outputs for the sake of conciseness. In Fig. 16, we show the wavelet sequences obtained after HDC processing of the traces less contaminated by noise (Fig. 15, upper part) and pairs of values: $t_0 = 0.3$ s, $V = 2500 \text{ m s}^{-1}$; $t_0 = 1.3$ s, $V = 800 \text{ m s}^{-1}$; and $t_0 = 2.5$ s, $V = 600 \text{ m s}^{-1}$. The detection of information is made on the set of wavelet sequences

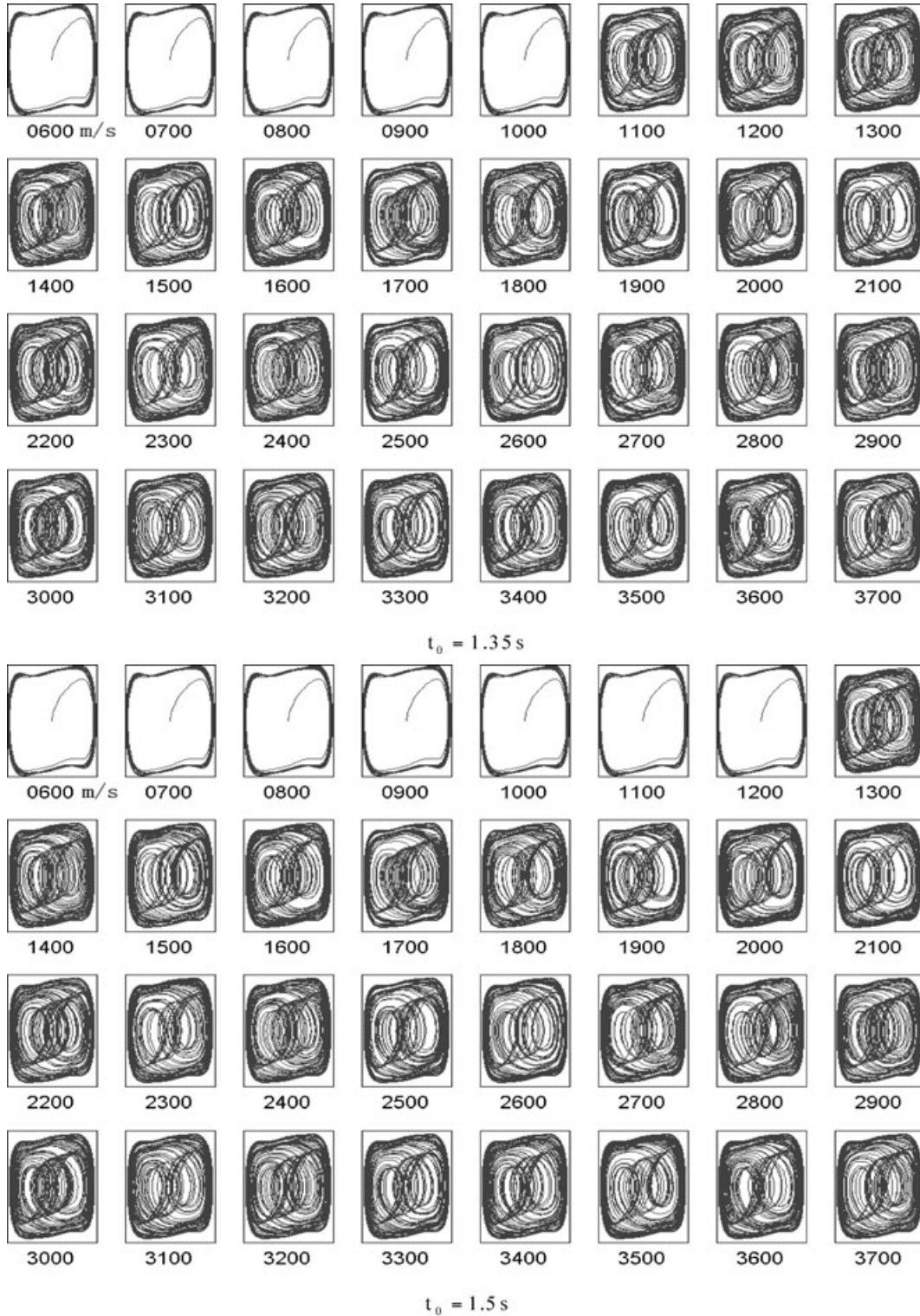


Figure 17. (Continued.)

obtained by HDC and solving eq. (4) to find out the phase state of the non-linear dynamic system. Fig. 17 groups together some representative configurations obtained from 32 scanning velocities and times: (a) $t_0 = 0.35, 0.40$ and 0.45 s for reflected waves type I;

(b) $t_0 = 1.25, 1.35$ and 1.50 s for waves type II; (c) $t_0 = 2.40, 2.45$ and 2.55 s for waves type III.

We follow the same process with respect to the other common shot record with traces strongly contaminated by noise (Fig. 15,

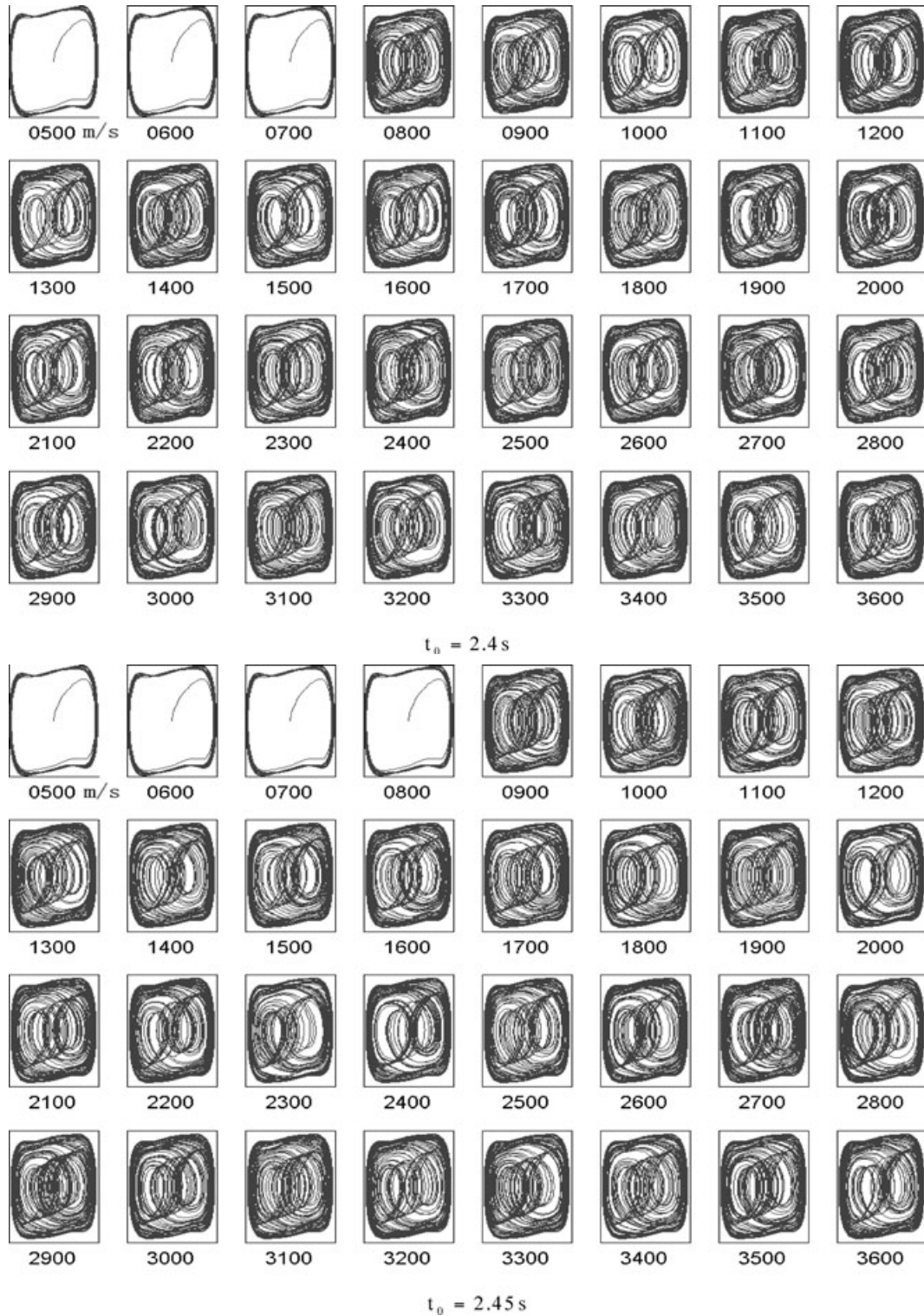


Figure 17. (Continued.)

lower part). Considering the fuzzy waveforms of the tested events, we now take seismic wavelet lengths of 70 ms in the range 0.1–0.7 s, 170 ms in the range 0.71–1.6 s, 110 ms in the range 1.61–3.0 s and 140 ms in the range 3.1–5.0 s. Fig. 18 shows the wavelet sequences obtained after HDC processing of the traces and pairs of

values: $t_0 = 0.3$ s, $V = 2400$ m s $^{-1}$; $t_0 = 1.3$ s, $V = 800$ m s $^{-1}$; and $t_0 = 2.1$ s, $V = 600$ m s $^{-1}$. As before, the detection of information is made on the set of wavelet sequences and investigating the phase state of the excited chaotic oscillator. Among the corresponding outputs obtained, Fig. 19 groups together some representative

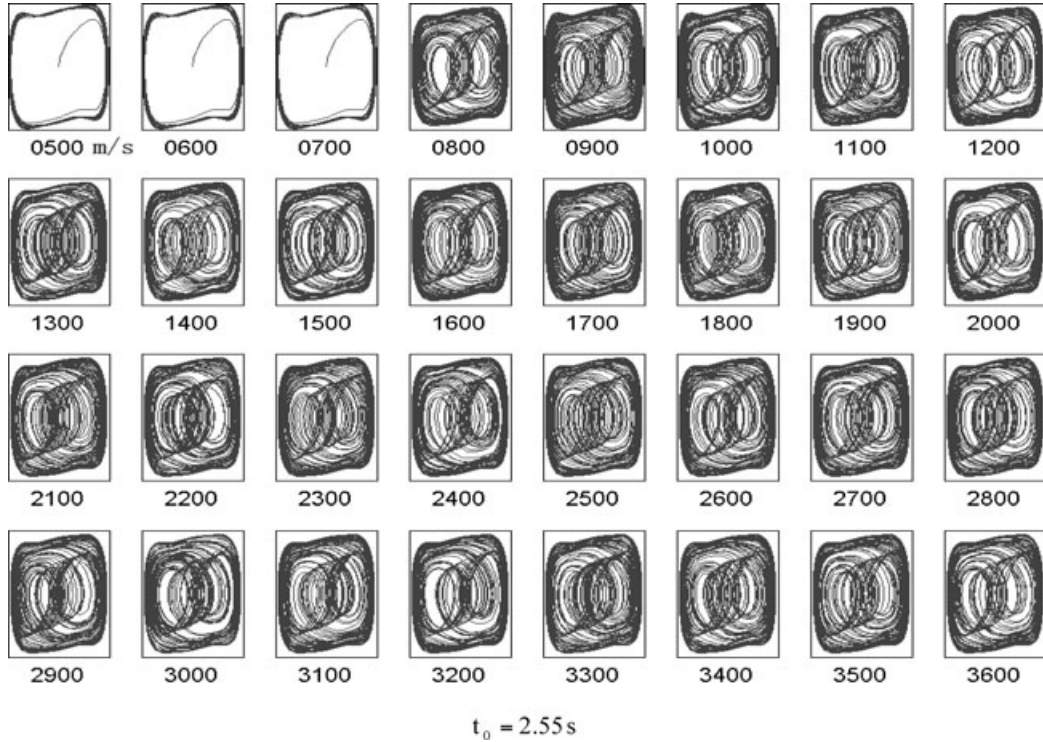


Figure 17. (Continued.)

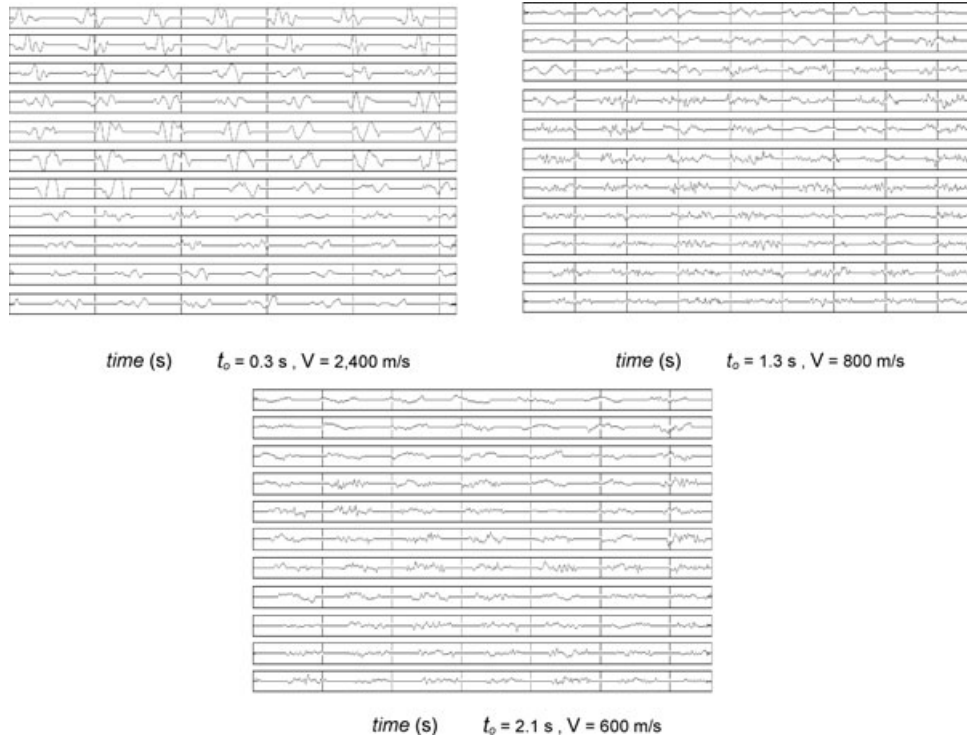


Figure 18. Wavelet sequences after applying the horizontal dynamic correction to the traces shown in Fig. 15 (lower part). As control times and velocities were taken: (a) $t_0 = 0.3$ s, $V = 2400$ m s $^{-1}$; (b) $t_0 = 1.3$ s, $V = 800$ m s $^{-1}$; and (c) $t_0 = 2.1$ s, $V = 600$ m s $^{-1}$.

configurations obtained from 32 scanning velocities and times: (a) $t_0 = 0.30, 0.35$ and 0.40 s for reflected waves type I; (b) $t_0 = 1.25, 1.30$ and 1.50 s for waves type II; (c) $t_0 = 2.45$ and 2.50 s for waves type III.

Similarity and repeatability are basic properties that a periodic signal must demonstrate. In Fig. 16 (shot A, $t_0 = 0.3$ s, $V =$

2500 m s $^{-1}$, periodic phase state) we can see 77 wavelets preserving these conditions, and therefore, the pseudo-periodicity of the signal because of the relatively weak random noise affecting the record (Fig. 15, upper part); 43 of them, from wavelet nos. 1 to 47 except wavelets nos. 9, 12, 19 and 20, consist roughly of two different distorted phases keeping both shape and apparent

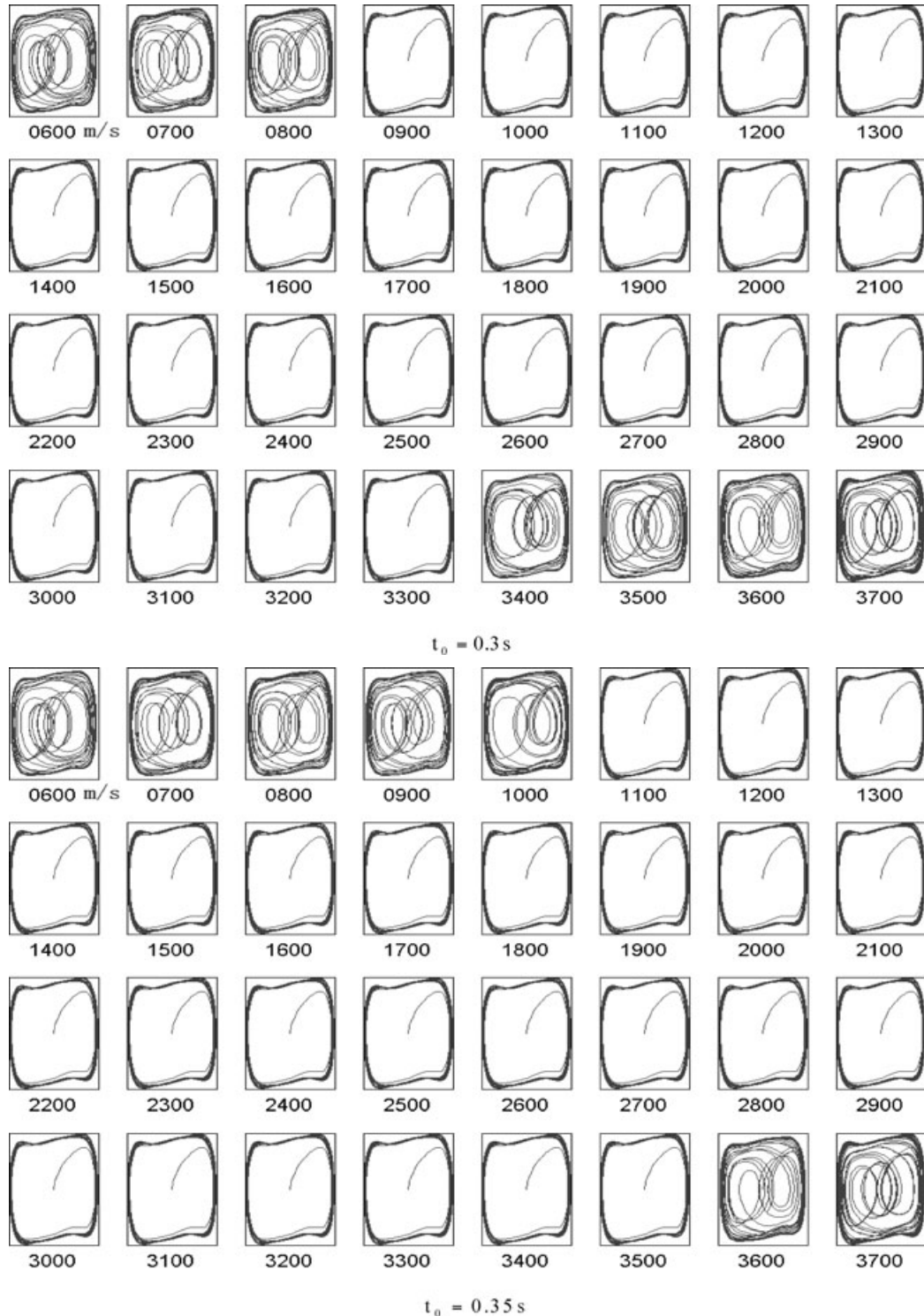


Figure 19. Orbit described by a same oscillator system (eq. 4) in the phase space showing different configurations obtained from 32 scanning velocities (from 600 to 3700 m s $^{-1}$) and various arrival times ($0.30, 0.35, 0.40, 1.25, 1.30, 1.35, 2.45$ and 2.50 s), with reference to possible reflection seismic events recorded after shot B (Fig. 15, lower part).

frequency. On the other hand, in Fig. 18 (shot B, $t_0 = 1.3$ s, $V = 800 \text{ m s}^{-1}$, chaotic phase state) such properties of the wavelets, and therefore, the pseudo-periodic character of the signal are rarely observed. In spite of this fact, wavelet sequences like those represented in Fig. 18 (shot B, $t_0 = 0.3$ s, $V = 2400 \text{ m s}^{-1}$; $t_0 = 1.3$ s, $V = 800 \text{ m s}^{-1}$; $t_0 = 2.1$ s, $V = 600 \text{ m s}^{-1}$) make feasible the system to reach the large-scale periodic phase state (Fig. 19). The reason may be a local similarity degree of the wavelets in some

cases, enough for the strong random noise (even as a serious distortion factor of waveforms) to be unable to destroy that similarity, the pseudo-periodicity of the signal remaining more or less preserved. Sometimes the periodicity of the wavelets, even as a fact, cannot be recognized in the data as it is hidden.

From the analysis of the many computed results (some of them illustrated in Figs 17 and 19) and the observation of large-scale periodic phase states of the excited dynamic system, we infer the

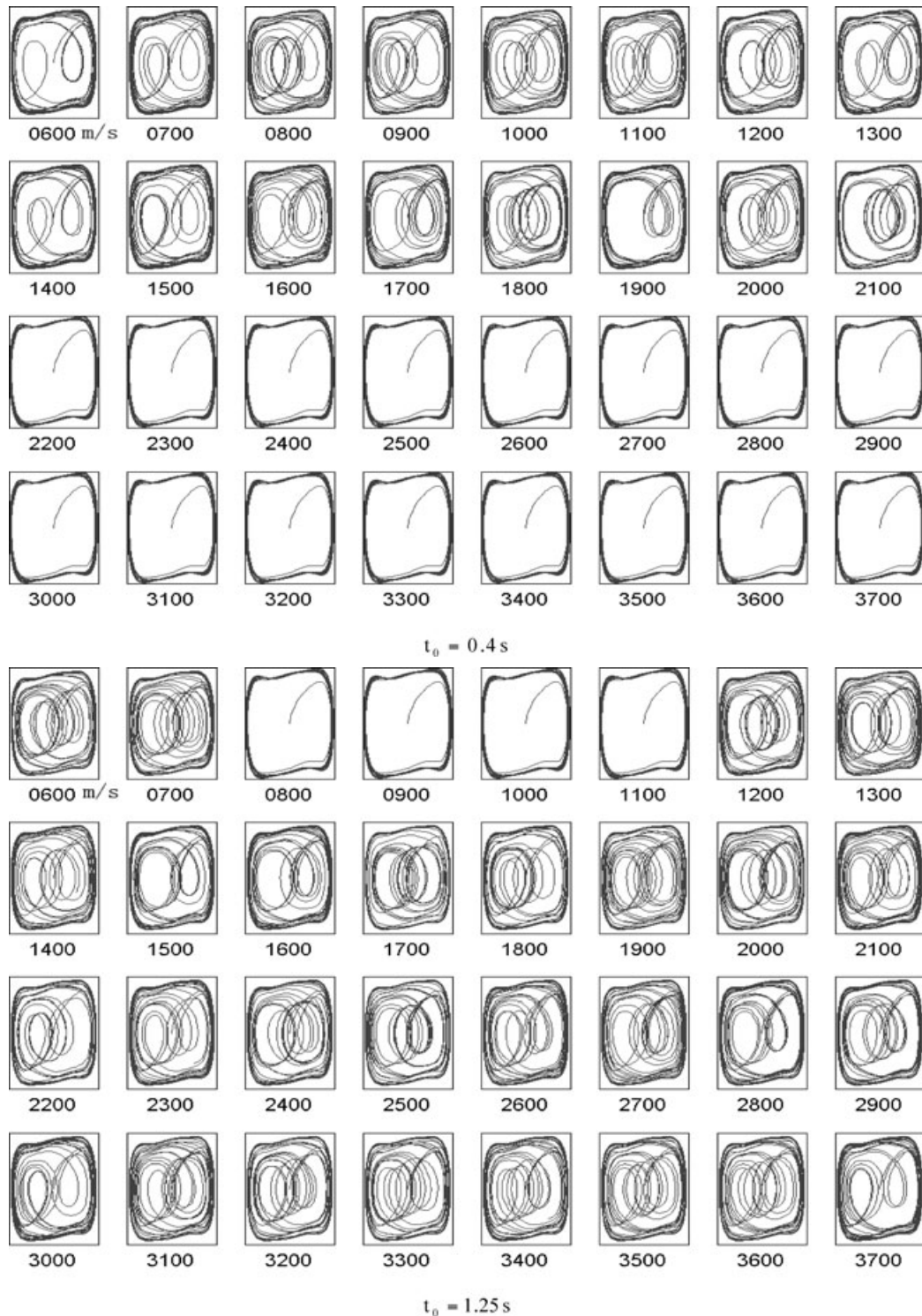


Figure 19. (Continued.)

existence of several solutions characterized by a rather high transmission (scanning) velocity in correspondence with real seismic events that are present in the two analysed record sections (from shots A and B). This inference must be viewed positively since it permits to ensure seismic reflections from real markers and too a variety of propagation velocities for these events, above all in relation with wave groups I and II, thus leaving different possibilities open to interpretation. However, this does not happen when dealing

with waves belonging to group III, which are present in the less contaminated data (shot A) and also in the noisy data (shot B). A closer view of the results allows us to say more about these delayed events in both records. Periodic phase states of the system corresponding to configurations $t_0 = 1.25, 1.35, 1.50$ s and similar states corresponding to configurations $t_0 = 2.40, 2.45, 2.55$ s (shot A, Fig. 17), demonstrate that the velocity V of the seismic phases classified as III is systematically less than the velocity V of the phases

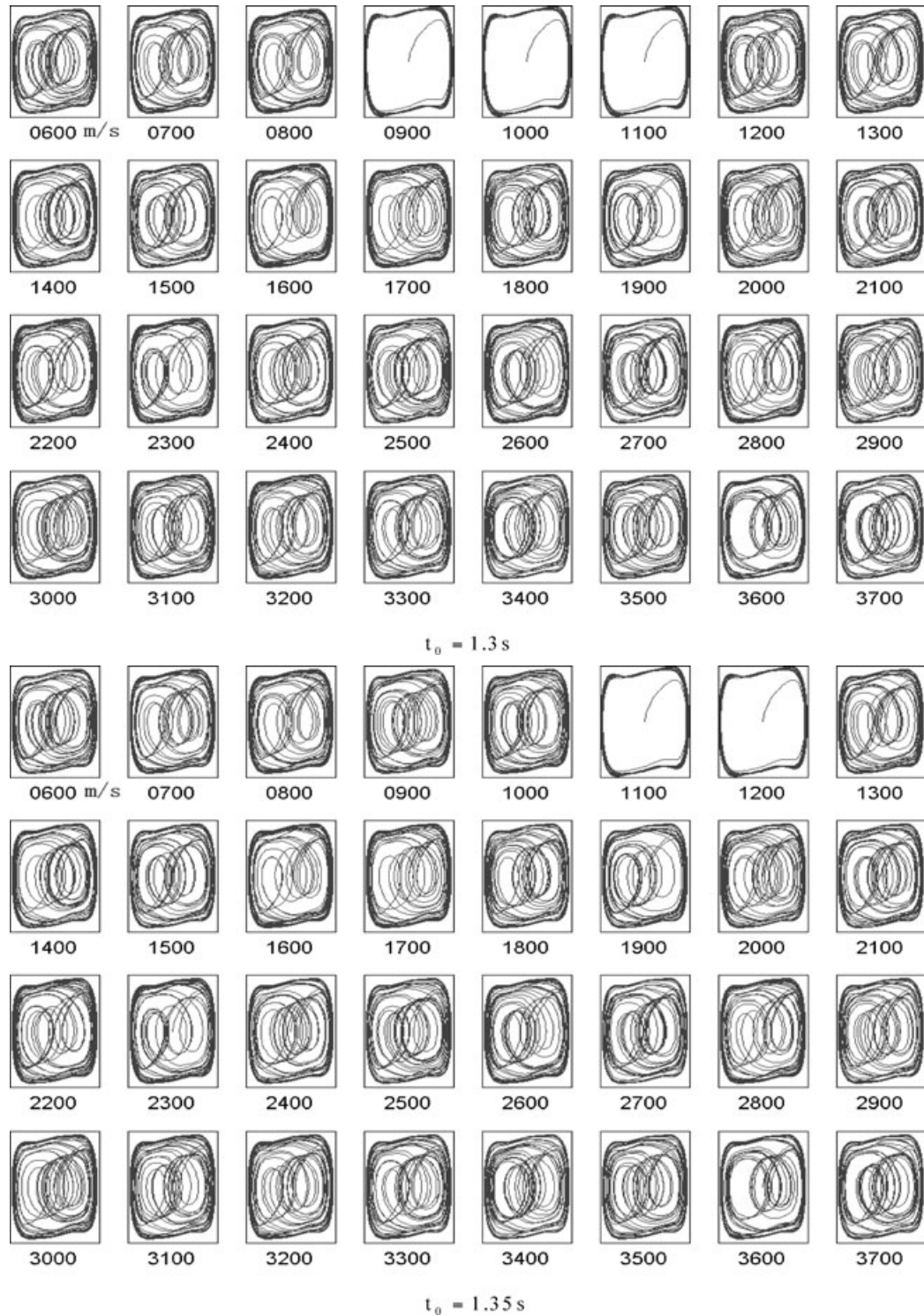
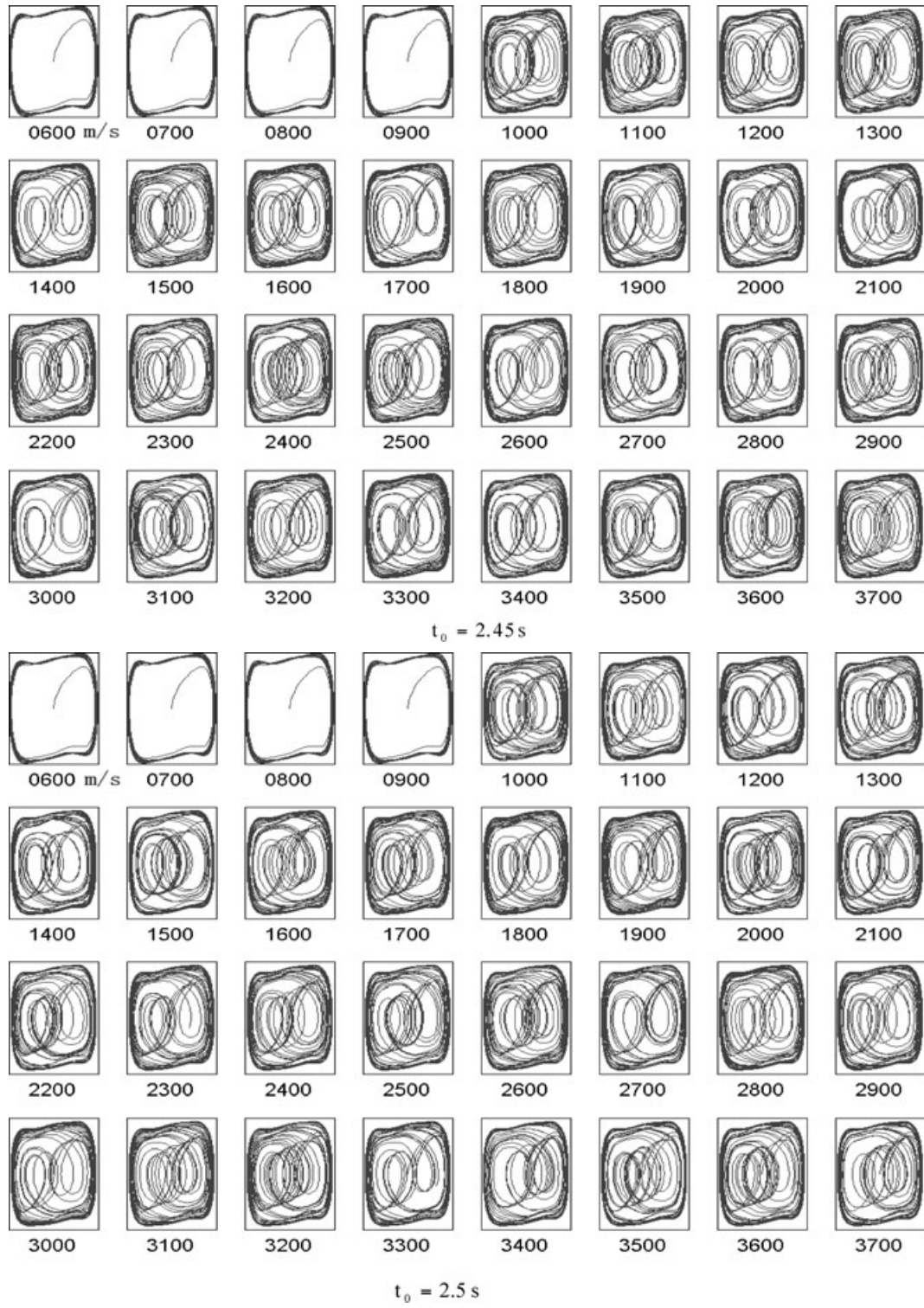


Figure 19. (Continued.)

**Figure 19.** (Continued.)

classified as II. Analogously when comparing configurations and periodic phase states for times $t_0 = 1.25, 1.30, 1.35 \text{ s}$ and $t_0 = 2.45, 2.50 \text{ s}$ (shot B, Fig. 19). In addition, the time t_0 for waves belonging to group III is above 2.2 s , obviously more than the time $t_0 \sim 1.8 \text{ s}$ for waves of group II (Fig. 15, lower part). Combining these results the conclusion is that the fuzzy waves labelled as type III may be discriminated as multiples generated between the near-

surface high-velocity layer and the reflecting interface origin of the waves reflected from the bottom of the basin and labelled as type II. To emphasize this conclusion concerning the traces after shot B (Fig. 15, lower part) even more, we have filtered that traces. Given that the traces exhibit certain dissimilarity and that the strength of the natural noise contaminating the signal is changing and unknown (unless a long record portion preceding the real seismic signal be

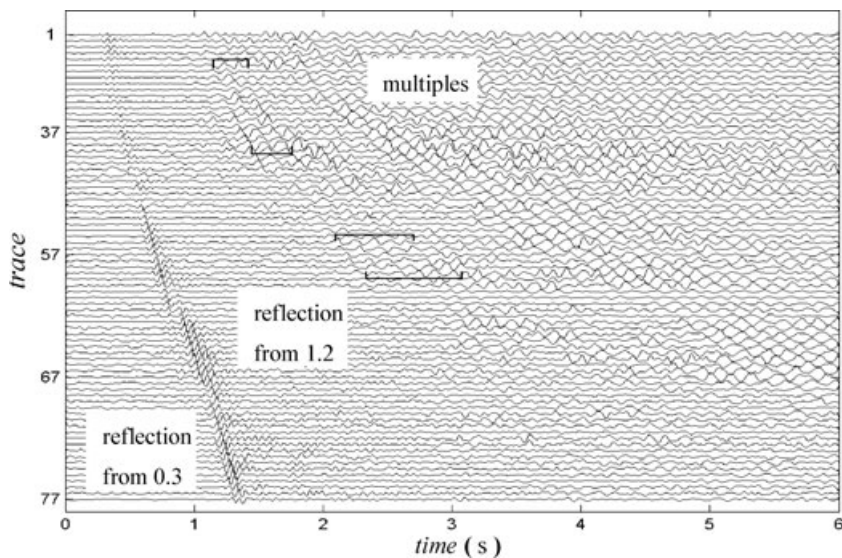


Figure 20. Filtered traces of the seismic record shown in Fig. 15 (lower part). A reflection from 0.3 s is very evident and may be clearly correlated along all traces. Other reflection from 1.2 s may be partially correlated for traces 7–21 and 36–41 (in brackets).

previously analysed), we have used time-frequency peak filtering (Boashash & Mesbah 2004; Jin *et al.* 2005) to increase the *S/N* ratio. The results obtained after filtering are shown in Fig. 20: as can be seen, a reflection event with arrival time t_0 near to 0.3 s (initially denoted as I) is very evident and can be clearly correlated along all traces; but also other reflection event with arrival time t_0 near to 1.2 s (initially denoted as II) coming from a deeper frontier appears partially defined for traces 7–21 and 36–41 (in brackets), with the number of peaks in the traces passing from two to five. As for a supposed third event with arrival time t_0 near 2.55 s, no combination of wavelets can be appreciated in the filtered traces, and therefore, it is not possible to confirm the existence of such an event.

8 CONCLUSIONS

The keystone for detecting a weak seismic signal in the context of non-linear science and chaos theory is the ‘immunity’ of a chaotic oscillator to high levels of random noise and its ability to change to a large-scale periodic phase state when excited by a periodic signal. The dynamic system can be controlled by a variety of non-linear equations offering different detection capabilities; however, we have used the Duffing–Holmes equation that contains the power x^5 in the restitution term to ensure sensitivity to any regular periodic signal.

The oscillations in the phase space described by a chaotic dynamic system excited by a distorted Ricker wavelet sequence as input signal demonstrate that it is possible to detect a weak event in a strong noise environment (-7.88 dB).

Events with *S/N* ratio less than -3 dB (1:2) or simply 0 dB (1:1) cannot often be recognized at first glance in common shot seismic records, but the chaotic detection method can be applied with success to this kind of noisy data. Since an event is really a 2-D signal due to its dependence upon both location and time, the prerequisite is that the original traces must be first converted into a wavelet sequence, i.e. into a pseudo-periodic seismic signal, by the so-called horizontal dynamic correction. This operation can be performed by placing all arrivals of the reflected seismic wavelets on

a single trace with a common reference time. The procedure requires the choice and testing of a set of arrival times and feasible scanning velocities for data processing, but even so it is relatively easy to be implemented with synthetic or real data. Anyhow, the possible fundamental weakness of the technique when using a particular scanning velocity is examined via the effect caused by near-surface lateral velocity variation on the periodicity of the reconstructed seismic signal. The numerical tests developed from several arrival times and scanning velocities support the power and reliability of the technique.

The presence of events in common shot records is confirmed as the system reaches a periodic phase state for admissible values of arrival time and transmission velocity, and hence, the advantages of the method to discriminate possible seismic reflections from other undesirable energy arrivals.

Chaotic system detection combined with digital filtering proves to be a useful tool to investigate seismic signals in noise environments characterized by low *S/N* ratio, for example exploration/industrial seismic signals and perhaps to detect weak earthquakes or underground test signals. All these potential applications may be of interest for seismologists who routinely apply linear signal processing techniques in data pre-processing.

ACKNOWLEDGMENTS

The research work here presented was taken up during a brief stay of one of the authors, JB, in the Jilin University of Changchun, Northern China. We would like to thank Profs Zhongjie Zhang and Enru Liu for their valuable suggestions and useful discussions. Helpful comments and criticism from the editor Dr Andrew Curtis and one anonymous referee that led to significant improvement of the paper are gratefully acknowledged. We thank Thomas Reppert for his impeccable assistance with English. The National Natural Science Foundation of China, Grant Nos. 40374045, 40774054 and 40574051 and the Science and Technology Development Project of Jilin Province, Grant No. 20050526, supported this research.

REFERENCES

- Anderson, R.M. & May, R.M., 1982. Directly transmitted infections diseases: control by vaccination, *Science*, **215**, 1053–1060.
- Benyamin, N., 2002. Key elements of total seismic field design using Mathematica—a tutorial, *Geophysics*, **67**, 1020–1027.
- Bernhardt, P.A., 1994. Communications using chaotic frequency modulation, *Int. J. Bifurcat. Chaos*, **4**, 427–440.
- Birx, D.I., 1992. Chaotic oscillators and CMFFNS for signal detection in noise environments, in *Proc. IEEE International Joint Conference on Neural Networks*, New York, Vol. 2, pp. 881–888.
- Boashash, B. & Mesbah, M., 2004. Signal enhancement by time-frequency peak filtering, *IEEE Trans. Signal Process.*, **52**, 929–937.
- Brandsberg-Dahl, S., de Hoop, M.V. & Ursin, B., 2003. Focusing in dip and AVA compensations on scattering-angle/azimuth common image gathers, *Geophysics*, **68**, 232–254.
- Ekren, B.O. & Ursin, B., 1999. True-amplitude frequency-wavenumber constant-offset migration, *Geophysics*, **64**, 915–924.
- Freybourger, M. & Chevrot, S., 2001. A waveform migration for the investigation of *P*-wave structure at the top of *D'* beneath northern Siberia, *J. geophys. Res.*, **106**(B3), 4129–4140.
- Guckenheimer, J. & Holmes, P., 1983. *Nonlinear oscillators, dynamical systems, and bifurcations of vector fields*, Springer-Verlag, New York, pp. 82–91 and 173–184.
- Harris, P.E. & White, R.E., 1997. Improving the performance of *f-x* prediction filtering at low signal-to-noise ratio, *Geophys. Prospect.*, **45**, 269–302.
- Haykin, S. & Li, X.B., 1995. Detection of signals in chaos, *Proc. IEEE*, **83**, 94.
- Hung, S.H. & Forsyth, D.W., 2000. Can a narrow, melt-rich, low-velocity zone of mantle upwelling be hidden beneath the East Pacific Rise? Limits from waveform modeling and the MELT Experiment, *J. geophys. Res.*, **105**(B4), 7945–7960.
- Jiao, L. & Moon, W.M., 2000. Detection of seismic refraction signals using a variance fractal dimension technique, *Geophysics*, **65**, 286–292.
- Jin, L., Li, Y. & Yang, B.J., 2005. Reduction of random noise for seismic data by time-frequency peak filtering (in Chinese with English abstract), *Progress Geophys.*, **20**, 724–728.
- Kelamis, P.G. & Verschuur, D.J., 2000. Surface-related multiple elimination on land seismic data-strategies via case studies, *Geophysics*, **65**, 719–734.
- Leung, H. & Huang, X.P., 1996. Parameter estimation in chaotic noise, *IEEE Trans. Signal Process.*, **44**, 2456–2463.
- Li, Y. & Yang, B.J., 2003. Chaotic oscillator system for detection of periodic signals under strong background noise, *Chin. Sci. Bull.*, **48**, 508–510.
- Linus, P., Friedemann, W. & Zhao, P., 1998. Prestack Kirchhoff depth migration of shallow seismic data, *Geophysics*, **63**, 1241–1247.
- May, R.M., 1974. Biological populations with nonoverlapping generations: stable points, stable cycles, and chaos, *Science*, **186**, 645–647.
- May, R.M., 1976. Simple mathematical models with very complicated dynamics, *Nature*, **261**, 459–467.
- May, R.M. & Anderson, R.M., 1979. Population biology of infectious disease, Part 2, *Nature*, **280**, 455–461.
- Moloney, J.V. & Newell, A.C., 1990. Nonlinear Optics, *Phys.D*, **44**, 1–37.
- Pecora, L.M. & Carroll, T.L., 1990. Synchronization in chaotic systems, *Phys. Rev. Lett.*, **64**, 821–824.
- Pecora, L.M. & Carroll, T.L., 1991. Driving systems with chaotic signals, *Phys. Rev. A*, **44**, 2374–2383.
- Quin, S. & Smythe, D.K., 1998. Filtering vibroseis data in the precorrelation domain, *Geophys. Prospect.*, **46**, 303–322.
- Selvi, O., 1997. Note on digital filtering with the second moment norm, *Geophysics*, **62**, 1315–1320.
- Sheriff, R.E., 1994. *Encyclopedic Dictionary of Exploration Geophysics*, 3rd edn, Society of Exploration Geophysicists, Tulsa.
- Short, K.M., 1997. Signal extraction from chaotic communications, *Inter. J. Bif. Chaos*, **17**, 1579–1597.
- Simmendinger, C. & Hess, O., 1996. Controlling delay-induced chaotic behavior of a semiconductor laser with optical feedback, *Phys. Lett. A*, **216**, 97–105.
- Soma, N., Niitsuma, H. & Baria, R., 2002. Reflection technique in time-frequency domain using multicomponent acoustic emission signals and application to geothermal reservoirs, *Geophysics*, **67**, 928–938.
- Spitzer, R., Nitsche, F.O. & Green, A.G., 2001. Reducing source-generated noise in shallow seismic data using linear and hyperbolic tau-p transformations, *Geophysics*, **66**, 1612–1621.
- Steeghs, P. & Drijkoningen, G., 2001. Seismic sequence analysis and attribute extraction using quadratic time-frequency representations, *Geophysics*, **66**, 1947–1959.
- Teitsworth, S.W., Westervelt, R.W. & Italler, E.E., 1983. Nonlinear oscillation and chaos in electrical breakdown in Ge, *Phys. Rev. Lett.*, **51**, 825–828.
- Teitsworth, S.W. & Westervelt, R.W., 1984. Chaos and broadband noise in extrinsic photoconductors, *Phys. Rev. Lett.*, **53**, 2587–2590.
- Tyapkin, Y.K. & Robinson, E.A., 2003. Optimum pilot sweep, *Geophys. Prospect.*, **51**, 15–22.
- Van Der Baan, M. & Paul, A., 2000. Recognition and reconstruction of coherent energy with application to deep seismic reflection data, *Geophysics*, **65**, 656–667.
- Van Der Heuel, J.C., Driesenaar, M.L. & Lerou, R.J.L., 2000. Fractal properties and denoising of lidar signals from cirrus clouds, *J. geophys. Res.*, **105**(D3), 3975–3982.
- Wang, G.Y., Chen, D.J., Lin, J.Y. & Chen, X., 1999. The application of chaotic oscillators to weak signal detection, *IEEE Trans. Ind. Electron.*, **46**, 440–443.
- Wang, Y., 2003. Quantifying the effectiveness of stabilized inverse Q filtering, *Geophysics*, **68**, 337–345.
- Weiss, C.O., Klische, W., Ering, P.S. & Cooper, M., 1985. Instabilities and chaos of a single mode NH₃ ring laser, *Opt. Commun.*, **52**, 405–407.